

3D NUMERICAL MODELS FOR ALONG-AXIS VARIATIONS IN DIKING AT
MID-OCEAN RIDGES

by

田小川

(Tian, Xiaochuan)

A Thesis

Submitted in Partial Fulfillment of the
Requirements for the Degree of
Master of Science

Major: Geophysics

The University of Memphis

May, 2015

Copyright © 2015 Xiaochuan Tian

All rights reserved

Dedication

I would like to dedicate this thesis to my mother, Xia Tian. I wouldn't have a chance to experience this wonderful world without her giving birth to me. She rears me up by herself with her great love, optimism and peseverence. Without her guidance and support, I will not become who I am.

I also want to dedicate this thesis toward my major thesis advisor: Dr. Eunseo Choi. His mentorship defines what a great advisor is like. Without his guidance, neither this theis nor my fast personal-development during these two years is possible. He has kindled a flame that illuminates the way for my future career as a geodynamic modeler.

Acknowledgements

There is no proper words for me to express my deep gratitude toward my thesis advisor Dr. Eunseo Choi. He has changed my life in a very positive way. From him, I have learned what a great researcher and educator should be like. It is because of his unfailing care and understanding that have given me the courage to persevere, to carry on during the darkest days as an international student far away from home. It is his vivid and interesting lessons that have inspired me so much that I want to devote my career into geodynamic modeling. It is his numerous inspiration and encouragement that has motivated me to work super hard (enjoy at the same time) on the fascinating research questions. It is his altruistic share that has provided me with great chances to learn from great researchers, references, and to attend meetings. It is his patience to guide me through my endless silly questions that has nourished and cultivated my capabilities of being an independent researcher. Blessings from Eunseo, my role model, are countless. I will keep them in mind and try my best to relay the torch.

To the other two committee members, Dr. Christine Powell and Dr. Jer-ming Chiu, for their guidance and advice during many committee meetings. For their interesting courses.

To Center for Earthquake Research and Information and University of Memphis, thank a lot for providing me this great chance to study here with full tuition and graduate research assistanship. It is this kind support that has made my two year studies at this great institution possible. To all the faculties taught me courses and staff Josephine provided me a very pleasant, tidy and clean place for doing research and studying.

To students, Yangyang Naeem Sabber

To Center for Writing and Communication staff: Bill Schraufnagel To Tianhe2 super computer center, thank a lot for the support from National Supercomputer Center in Guangzhou. For about 200k Sus.

To Dr. Jie Liu and Dr. Ke Zhang, for kindly sharing their computing resources on Tianhe2.

To Dr. Gu Cheng,

To Shengfang Chen and Lijie Lyu

Finally, I want to thank my families, grandfather, grandgrandfather(ling zhong qian rang wo hao hao xue xi), grandma, mum.

“In the midst of winter, I found there was, within me, an invincible summer.”

—Albert Camus

“People have no higher calling than to strive for the greater good of humankind and society and that the future of humanity can be assured only when there is a balance between scientific development and the enrichment of the human spirit.”

—Kazuo Inamori

“不失其所者久，死而不亡者寿。”

—《道德经》

Abstract

Tian, Xiaochuan. M.S. The University of Memphis. May 2015 Master of Science.
3D Numerical Models for Along-axis Variations in Diking at Mid-Ocean Ridges. Major
Professor: Eunseo Choi.

Bathymetry of ocean floors reveals a great variety of morphologies at Mid-ocean Ridges (MORs). Previous studies showed that the morphologies at slow spreading MORs are mainly controlled by the ratio between rates of magma supply and plate extension. 2D models for the across-ridge cross-sections have been successful in explaining many of the observed morphological features such as abyssal hills and oceanic core complexes. However, the magma supply varies along the ridge and the interaction between the tectonic plates and magmatism at MORs are inevitably 3D processes. We propose to investigate the consequences of the along-axis variability in diking in terms of faulting pattern and the associated structures. This work will include implementation of an algorithm of parameterizing repeated diking in a 3D parallel geodynamic modeling code.

Table of Contents

Chapter	Page
1 Introduction	1
1.1 Review of Literature	1
1.2 Statement of Research Purpose	6
2 Methods	7
2.1 Method of approach	7
2.2 Model Setup	8
2.3 Parameters to control	9
3 Results	13
3.1 Reference model M28LinT1	13
3.1.1 Constant M along the ridge axis (M88ConT2 Table 2)	17
3.2 Main characteristics of the models	18
3.2.1 Location of termination	19
3.2.2 Geometry of the trough	20
3.2.3 Inward fault jump	20
3.2.4 Fault alternation	21
3.2.5 Cut-back	21
3.2.6 Hourglass shape median valley	25
3.2.7 Corrugations and mullion structures	27
3.3 Effects of the functional forms of M variation	29
3.4 Effects of the weakening rate	31
3.4.1 M58SinT1 versus M58SinT2	34
3.4.2 M58SqrtT1 versus M58SqrtT2	37
3.5 Effects of the range of M variation	40

3.5.1	M28SinT1 versus M57SinT1 versus M58SinT1	40
3.5.2	M57SinT2 versus M58SinT2	42
3.5.3	M28LinT1 versus M57LinT1	42
3.5.4	M28SqrtT1 versus M58SqrtT1	43
3.5.5	M57SqrtT2 versus M58SqrtT2	44
3.6	Summary of Results	45
4	Discussion	47
4.1	Discussion on Reference models	48
4.2	Fault Alternation	48
4.2.1	Trade-off between bending and weakening	48
4.2.2	Alternating on conjugate plate	49
4.2.3	Secondary near-axis normal fault	50
4.2.4	Effect of along ridge-axis coupling	50
4.3	Corrugations	51
4.3.1	Wavelength of corrugations	51
4.4	Influence of healing	51
4.5	Comparing model results with nature observation	51
4.5.1	Cut back at 13°N Mid-Atlantic Ridge (M28SqrtT1)	51
4.5.2	Double dome at 23°N Mid-Atlantic Ridge (Kane Megamullions) (Several models)	52
4.5.3	Atlantis Massif Shape at 30°N Mid-Atlantic Ridge ()	53
4.5.4	Shear low	53
4.5.5	Corrugations	53
4.6	Model Limitation	53
4.6.1	Fixed thermal structure effects and justification	53
4.7	Recommendation for Future Research	53

5 Conclusions **54**

Bibliography **55**

List of Tables

1	Summary of 3D Model Parameters	11
2	List of 3D numerical experiments.	12
3	Model behaviors in short.	45
4	Linear functional form.	46
5	Sinusoidal functional form.	46
6	Square root functional form.	46

List of Figures

1	Profiles of bathymetry across MORs.	2
2	Two bathymetric profiles across the Mid-Atlantic Ridge around 30°N with ^{EC:} 10 times vertical exaggeration vertical exaggeration of 10 . A-A' is closer to the segment center while B-B' is at the tip of the segment. ^{EC:} near the Atlantis Transform fault ^{EC:} [If you want, add a label for this transform fault on the map.]	2
3	Relationship between the maximum crustal thickness variations (ΔH_c) along a ridge segment and the segment length (L). The dashed line is the best-fit linear regression of the combined data. [Chen and Lin, 1999]	3
4	Upper one: modeling result for fast spreading agrees well with the observation of East Pacific Rise. Lower one: modeling result for slow spreading ridges agrees well with the bathymetry of Mid Atlantic Ridge. [Buck et al., 2005]	4
5	A~F: Faulting behaviors for different values of M. Geologic interpretation is superimposed on modeled distribution of strain rate. Dots show breakaways of initial faults. Dashed seafloor is original model seafloor, red dotted seafloor is formed dominantly by magmatic accretion, and solid bold is fault surface. Note that the detachment faults in B and C are not interrupted by secondary faults. [Tucholke et al., 2008]	5
6	Essential components of the numerical method.	8
7	Model setup	9
8	Evolution of plastic strain and surface topography of the reference model M28LinT1 (Table 2). Each snapshot shows plastic strain plotted on the model domain and the five times exaggerated topography. Initial seafloor is marked as a reference of 0 km of the topography. The bold dash lines (black) are the terminations of the detachment faults. The bold dash lines (red) in g) and h) are the transfer faults that connect the terminations along the ridge. The inset in f) plots plastic strain with opacity linearly proportional to its value.	13

9	Bird's-eye view of the evolution of breakaway (marked by green bold line) and depressed narrow zone along the ridge axis ("trough") (red dash line in (a)) for model M28LinT1 (Table 2). This figure share the same color scales with Figure 8.	14
10	Bending stress illustration. The blue line is the neutral plane where $\sigma_{xx} = 0$. Above the neutral plane is compression ($\sigma_{xx} < 0$) and beneath it is tension ($\sigma_{xx} > 0$).	15
11	Bird's-eye view of velocity field with plastic strain plotted with opacity linearly proportional to its value. (color scale the same as Figure 8.a))	17
12	Bird's-eye view of σ_{xz}	17
13	Evolution of plastic strain and surface topography of the model: M88ConT2 (Table 2).	18
14	Five slices of strain rate along the ridge for the model M28LinT1 (Table 2) at 107.5 kyr. Terminations and breakaways along the ridge are marked by the black and red arrows respectively.	19
15	The weak detachment fault tip reaches the pre-existing shear stress at 160 kyr (M28SqrtT1) (Table 2).	21
16	Velocity field of M28SqrtT1 at 162.5 kyr. Magnitudes of the velocity are shown by the colors of the arrow heads. Plastic strain is plotted with opacity linearly to its value.	22
17	M28SqrtT1 (Table 2). Cut back behaviors in square root functional form model with different time.	23
18	Along ridge axis σ_{xz} (bird's-eye view of three layers of model domain) (positive(red) means clockwise) for M28SqrtT1 at 160 kyr. (Table 2). Plastic strain is plotted with opacity linearly proportional to its value.	24

19	M28SqrtT1 (Table 2). Bending stress drop (a versus b) at the lower M side due to the cut-back. No bending stress drop (c versus d) at the higher M side as a comparison.	25
20	M28SqrtT1 (Table 2). New fault front chase after initial abandoned breakaway.	25
21	Bird's-eye view of the evolution of the hourglass shape median valley.	26
22	Higher σ_{xx} shows inside the median valley on the negative x -axis direction of the ridge axis.	26
23	Bird's-eye view of the evolution of the corrugations. Color scales for the topography is the same as Figure 8.	27
24	Evolution of mullion structures. Color scales for the topography and the plastic strain are the same as Figure 8.	29
25	Three functional forms of M variation comparison. They begin to exceed the M= 0.5 black line at Z=10, 7, 5 for linear, sinusoidal and square root respectively.	30
26	M28LinT1 versus M28SinT1 (Table 2). Secondary fault length comparison between linear and sinusoidal. Around 13 elements in length for sinusoidal compared to 11 elements for linear.	31
27	M28LinT1 versus M28SqrtT1 (Table 2) at 97 kyr. View from top of the model.	32
28	M28LinT1 versus M28SqrtT1 (Table 2) at 100 kyr. View from top of the model.	33
29	M57SinT2 versus M57SinT1 (Table 2). a) and b) are for M57SinT2, c) and d) are for M57SinT1.	34
30	M57SinT1 (Table 2) faulting and stress evolution with respect to time.	35
31	M57SinT2 (Table 2) faulting and stress evolution with respect to time.	36
32	M58SinT1 (Table 2) faulting and stress evolution with respect to time.	37
33	M58SinT2 (Table 2) faulting and stress evolution with respect to time.	38
34	M58SqrtT1 (Table 2) faulting and stress evolution with respect to time.	39
35	M58SqrtT2 (Table 2) faulting and stress evolution with respect to time.	40

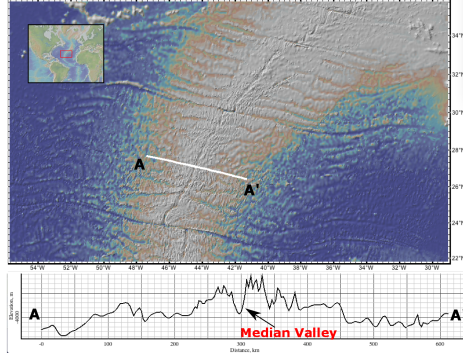
36	M28SinT1 (Table 2) faulting and stress evolution with respect to time.	41
37	M57LinT1 (Table 2) faulting and stress evolution with respect to time.	43
38	M57SqrtT2 (Table 2) faulting and stress evolution with respect to time.	44
39	Trade-off between change in bending force ΔF_b and weakening in the fault interface ΔF_w . H is the thickness of the brittle crust and γ is the size of initial weak perturbation and A defines the maximum bending force change. (For more details, please refer to [Lavier et al., 2000])	48
40	Comparing nature observation at 13°N Mid-Atlantic Ridge to the Cut back behavior of model M28SqrtT1. The model topography is a mirror symmetric flip according to the dash line, it reveals the case of M varies in a square root functional form from 0.2 to 0.8 to 0.2. For discussion on cut back formation mechanism, please refer to Section ?? . The bathymetry is from GeoMapApp [Ryan et al., 2009].	51
41	Comparing nature observation at 13°N Mid-Atlantic Ridge to the Cut back behavior of model M28SqrtT1. The model topography is a mirror symmetric flip according to the dash line, it reveals the case of M varies in a square root functional form from 0.2 to 0.8 to 0.2. For discussion on cut back formation mechanism, please refer to Section ??	52

1 Introduction

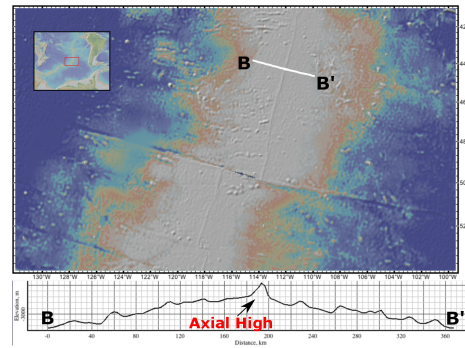
Around 70% area of the Earth's crust is the oceanic crust. New oceanic crust is constantly forming at the mid-ocean ridges (MORs), the longest mountain chains on the Earth. Seismic and volcanic activities are frequently happening along the MORs due to incessant seafloor spreading and magma upwelling. The interactions between the tectonics and magmatism along the MORs are considered to be responsible for the variations in the seafloor ^{EC:}topography [morphology would be more generic and thus better in this context.]. Geodynamic modeling along with a variety of geological, geophysical observation and lab experiment constraints have been used to study how does the interaction system between tectonics and magmatism at the MORs work under geological time scale ^{EC:} [Add some references].

1.1 Review of Literature

According to [Fowler, 2004], variations in mid-ocean ridge morphologies are mainly controlled by four factors: magma supply, tectonic strain, hydrothermal circulation and spreading rate.^{XT:}Clarify the relationship between the four factors and try to cite the original work for each of them. (in Fowler2004, they didn't mention the ref for these four factors, page417 Chapter9.4.1) Among them, the spreading rate shows the strongest correlation with the ridge morphology. Slow-to-intermediate spreading ridges (half spreading rate less than 4 cm/yr) produce median valleys that are typically 10~20 km wide and 1~2 km deep (e.g., Mid-Atlantic Ridges, Fig. 1a). Fast-spreading ridges (half spreading rate greater than 5 cm/yr) like the East Pacific Rise have axial highs that are 10~20 km wide, 0.3~0.5 km high (Fig. 1b).



(a) Slow spreading Mid-Atlantic Ridge



(b) Fast spreading East Pacific Rise

Figure 1: Profiles of bathymetry across MORs.

Slow spreading ridges exhibit along-axis variations in the width and depth of median valleys, crustal thickness and off-axis morphology. Figure 2 shows that the topographic profile near to the center of the ridge segment (A-A') is rather symmetric and has higher frequency. The maximum relief is about 1 km. In contrast, the near-tip profile (B-B') is asymmetric, has much lower frequency, and shows a greater relief (~ 3 km). The maximum along-axis variation in crustal thickness ΔH_c is linearly increasing with segment length L [Chen and Lin, 1999] and the relationship is $\Delta H_c(L) = 0.0206L$ (Figure 3).

EC: [Discussion on off-axis morphology is missing.]

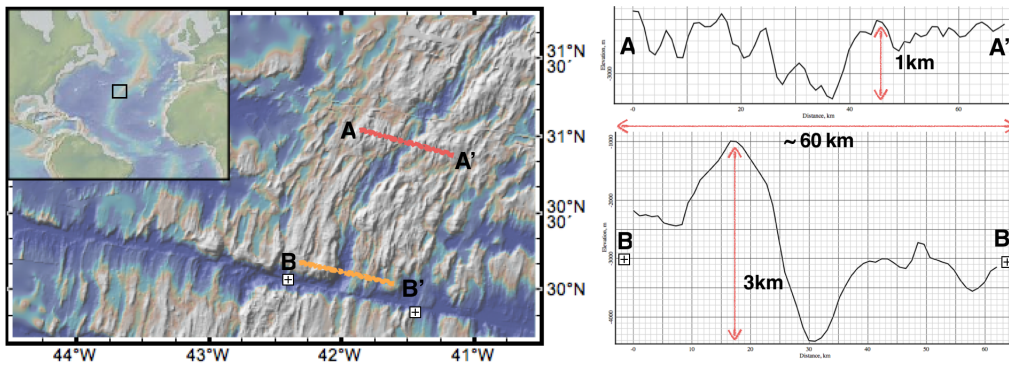


Figure 2: Two bathymetric profiles across the Mid-Atlantic Ridge around 30°N with *EC:* 10 times vertical exaggeration. A-A' is closer to the segment center while B-B' is at the tip of the segment. *EC:* near the Atlantis Transform fault *EC:* [If you want, add a label for this transform fault on the map.]

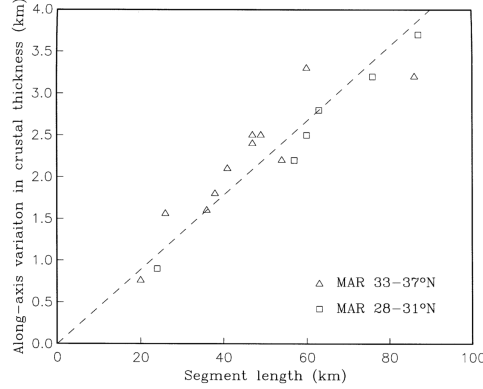


Figure 3: Relationship between the maximum crustal thickness variations (ΔH_c) along a ridge segment and the segment length (L). The dashed line is the best-fit linear regression of the combined data. [Chen and Lin, 1999]

Magma supply at MORs is mostly a passive process when no hot plume is present [Fowler, 2004]. Hot mantle rises up to fill the vacated room being created by plate separation and decompression leads to partial melting of the hot mantle. The melt upwells due to both pressure difference and buoyancy from lateral density difference. When the melt solidifies near the surface, it forms new crust. Melt can also feed dikes at the spreading center. Diking releases extensional stresses resulting from far-field forces (e.g. slab pull) that drive seafloor spreading.

The passive nature of magma upwelling at MORs leads to the major difference between fast and slow spreading ridges in the amount of magma supply. *EC: [Revise the rest of this paragraph. It's a repetition of the previous paragraph and not a proper explanation of the first sentence of this paragraph.]* At the fast spreading ridges, the rate of creating new space is greater than at the slow spreading ridges such that passive magma upwelling is also more supply is always sufficient for dikes to accommodate plate separation. However, the amount of magma supplied in the form of dikes at the slow spreading ridges and the oceanic lithosphere experiences internal deformations (i.e. tectonics process like normal faulting) when the accumulated extensional stress exceeds the strength of the crust.

Buck et al. [2005] attributed the contrasting faulting patterns and ocean floor morphology of fast- and slow-spreading ridges to the difference in the amount of diking-

accommodated plate extension. They defined the ratio between the rates of diking and plate separation as $M = V_{dx}/2V_x$, where V_{dx} is the rate of opening by diking at a MOR and V_x is the half spreading rate of the MOR. According to this definition, $M = 1$ represents the case where dike injection is so frequent that magma supply is sufficient to release all the tensional stresses from plate separation. $M = 0$ corresponds to the case of no magma supply, in which diking does not account for any of the plate motion and therefore plates kinematics requires plates to go through internal deformations. As shown in Figure 4, an axial high forms at a fast spreading ridge ($M = 1$) due to buoyancy from lateral density difference across ridge axis but a median valley forms at a slow-spreading ridge ($M = 0.5$) due to near-axis normal faulting, which is in turn caused by the stretching of oceanic lithosphere.

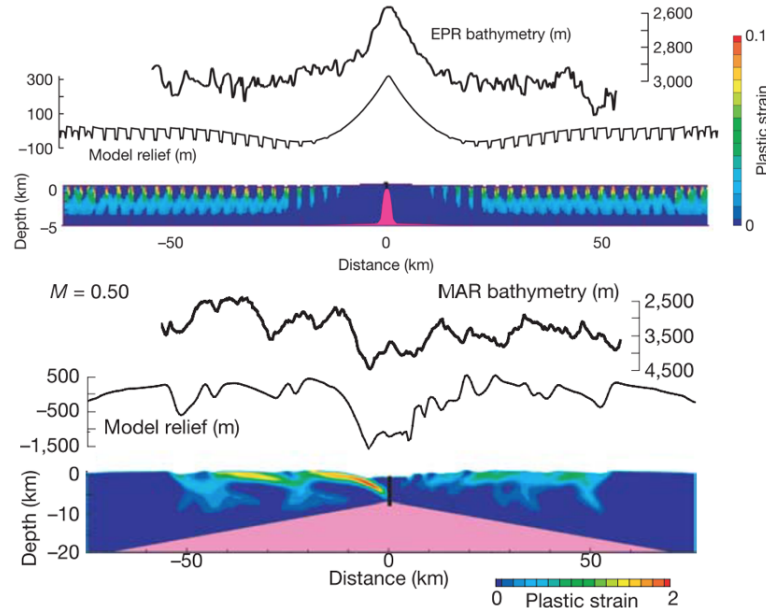


Figure 4: Upper one: modeling result for fast spreading agrees well with the observation of East Pacific Rise. Lower one: modeling result for slow spreading ridges agrees well with the bathymetry of Mid Atlantic Ridge. [Buck et al., 2005]

Tucholke et al. [2008] expand the investigation on the role of M in the mid-ocean ridge mechanics. They focus on the faulting behaviors of slow spreading ridges and find that the OCCs are most likely to form when M varies from 0.3 to 0.5. When $M = 0.7$

(Fig. ??A), repeated diking pushes faults that have formed at the spreading center away from the ridge axis. Since the thickness of the brittle layer increases away from the ridge axis, frictional and bending energy for maintaining the fault also increases. When the energy needed for maintaining an existing fault exceeds the energy for breaking a new near-axis fault, the old fault will cease to be active and the new one starts to accommodate extension. When $M = 0.3\sim0.5$, the normal fault remains active for a long time and rotates to a very low angle normal fault (detachment fault), exhuming the lower crust and mantle materials to the seafloor. When M is less than 0.3, most of the tension is accommodated by intra-plate deformations rather than by diking and as a result, faulting pattern is more complicated and unsteady.

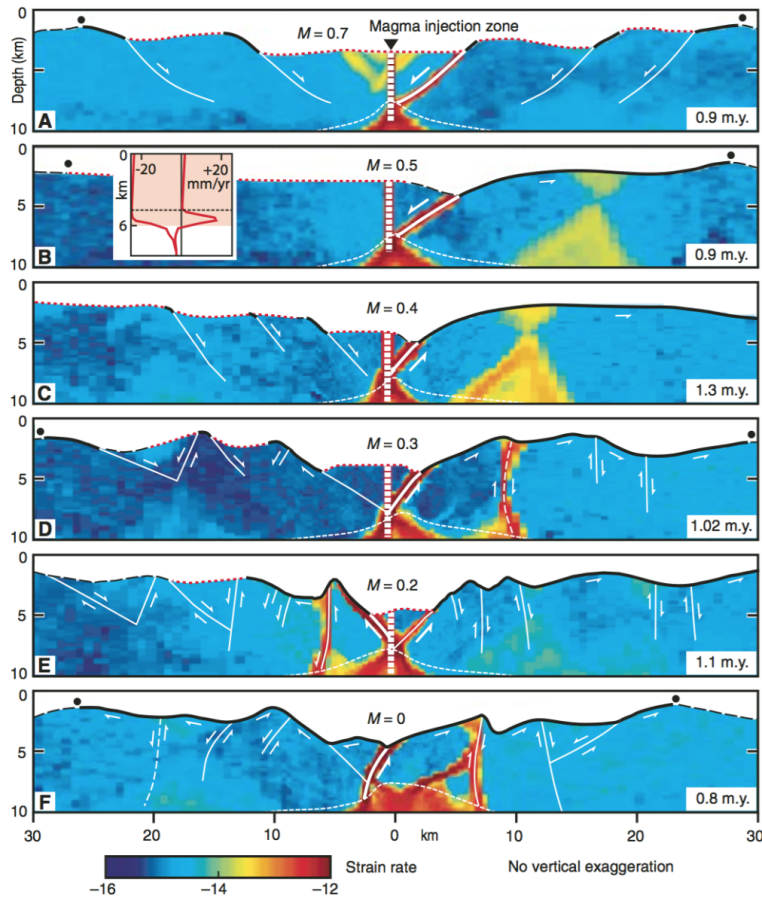


Figure 5: A~F: Faulting behaviors for different values of M . Geologic interpretation is superimposed on modeled distribution of strain rate. Dots show breakaways of initial faults. Dashed seafloor is original model seafloor, red dotted seafloor is formed dominantly by magmatic accretion, and solid bold is fault surface. Note that the detachment faults in B and C are not interrupted by secondary faults. [Tucholke et al., 2008]

1.2 Statement of Research Purpose

The M-factor formulation used in the previous 2D models [Tucholke et al., 2008, Buck et al., 2005] successfully explained major features found in across-ridge profiles of seafloor bathymetry. However, 2D models have limitations in studying the along-ridge variations in morphology and faulting patterns. Magma supply at fast spreading ridges seems always sufficient for accommodating plate motions with little variation along the ridge axis. The relatively uniform topography along fast spreading ridges is considered to be consistent with the uniform abundance of the magma supply. However, along the slow spreading ridges, bathymetry, gravity anomaly and results from reflection and refraction seismology show strong correlation with variation in crustal thickness [Ryan et al., 2009, Chen and Lin, 1999, Lin et al., 1990, Tolstoy et al., 1993]. Because oceanic crust is mainly formed by upwelled magma at the ridge, variation in the thickness of the crust implies variation in magma supply. At slow spreading ridges, the degree of cooling by hydrothermal circulation, thermal structures and even local spreading rate [Baines et al., 2008] also varies both along and across the ridge axis and they appear interrelated. Thus, for slow-to-intermediate spreading ridges, the interactions between tectonics and magmatism at MORs are inevitably 3D processes and 3D numerical models are desirable for better understanding factors controlling both across- and along-ridge topography variations.

The purpose of this thesis is to extend the M-factor formulation originally developed for 2D models to 3D by implementing it into a 3D numerical modeling code SNAC (StGermaiN Analysis of Continua) [Choi et al., 2008]. By systematically exploring the behaviors of the 3D models and comparing them with observations, we will be able to better understand how the mid-ocean ridge magmatism and tectonic deformations interact.

2 Methods

2.1 Method of approach

The numerical modeling code, SNAC, is an explicit Lagrangian finite element code that solves the force and energy ~~XT: find out which one is energy balance equation~~ balance equations for elasto-visco-plastic materials. Figure 6 shows major parts of the SNAC's algorithm.

For each time step of 0.5 yr, strain and strain rates are updated based on the initial or previous velocity fields under the constraints from boundary conditions. A constitutive model returns updated stresses corresponding to these deformation measures. Internal forces are then calculated from the updated stresses, which is plugged into the momentum balance equation together with the body force term. Then, the damped ~~XT: better understand the damped force~~ net force divided by inertial mass yields acceleration at a node point, which is time-integrated to velocity and displacement.

A 3D domain is discretized into hexahedral elements, each of which is in turn divided into two sets of tetrahedra. This symmetric discretization prevents faulting from favoring a specific direction or “mesh grains”.

Rheology for the oceanic lithosphere is assumed to be elasto-visco-plastic (EVP). When viscosity is high at low temperature, the rheology essentially becomes the Mohr-Coulomb plasticity with strain softening and thus can create shear bands that behave like faults. Strain softening is realized by cohesion decreasing with increasing amount of permanent (i.e., plastic) strain. I assume this relationship is linear for simplicity such that it is sufficient for a full description of strain weakening to define initial and final values of cohesion and a critical plastic strain at which cohesion becomes the final value. I define the rate of strain weakening as the cohesion difference divided by the critical plastic strain and use it as one of the model parameters. When temperature is high and viscosity is low, the rheology becomes the Maxwell viscoelasticity and can model creeping flow.

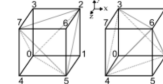
This property of the EVP model makes it possible to set up a structure with a brittle lithosphere and a ductile asthenosphere through a proper temperature distribution. Rheological parameters are taken from previous studies that use a similar rheology [e.g., [Buck et al., 2005](#); [Tucholke et al., 2008](#)] or from lab experiments [e.g., [Kirby and Kronenberg, 1987](#)].

For 3D diking processes, the expanding strain $\Delta\varepsilon_{xx}$ results from diking at the ridge leads to extra-stresses $\Delta\sigma_{xx}$, $\Delta\sigma_{yy}$ and $\Delta\sigma_{zz}$ in all three directions based on the linear elastic constitutive equations $\sigma_{ij} = \lambda\varepsilon_{kk}\delta_{ij} + 2\mu\varepsilon_{ij}$.

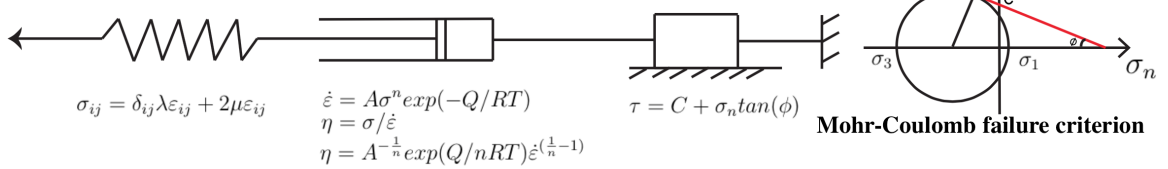
SNAC: a 3D, MPI parallelized, updated Lagrangian explicit finite difference code for modeling long-term tectonic evolution of the Earth's elasto-visco-plastic crust and mantle. (Choi et al., 2008)

Momentum Balance Equation: $\frac{\partial\sigma_{ij}}{\partial x_j} + \rho g_i = \rho \frac{Dv_i}{Dt}$

Spatial Decritization: A 3D domain is discretized into hexahedral elements, each of which is filled with two sets of 5 tetrahedra.



Elasto-Visco-Plastic (EVP) Rheology:



Diking M Formulation: $M = Vdx / 2Vx$ (Vdx is the dike accretion strain(dike widening) $\Delta\varepsilon_{xx}$ in each time step dt)

Stresses introduced by a dike accretion strain(dike widening) $\Delta\varepsilon_{xx}$ in each time step dt:

$$\Delta\sigma_{xx} = (\lambda + 2\mu)\Delta\varepsilon_{xx} \quad \Delta\sigma_{yy} = \lambda\Delta\varepsilon_{xx} \quad \Delta\sigma_{zz} = \lambda\Delta\varepsilon_{xx}$$

Figure 6: Essential components of the numerical method.

2.2 Model Setup

The 3D models has a geometry of $(60 \text{ km} \times 20 \text{ km} \times 20 \text{ km})$ in x , y and z axes respectively with a resolution of $\Delta x = 1 \text{ km}$ (Δx is the size of each hexahedron element). For comparison with the previous 2D models [e.g., [Buck et al., 2005](#); [Tucholke et al., 2008](#)], I also run pseudo-2D models and they have a geometry of $(60 \text{ km} \times 20 \text{ km} \times 1 \text{ km})$ in x , y and z axes respectively with a resolution of $\Delta x = 0.5 \text{ km}$. As shown in Figure 7, the initial temperature field linearly increases from 0°C at the top surface to 240°C at the depth of 6 km, reflecting enhanced cooling due to hydrothermal circulation. Below 6 km, the

temperature profile follows the semi-infinite half-space cooling model of moving plates [e.g., Turcotte and Schubert, 2002]. Two sides perpendicular to the z coordinate axis are free-slip. The top surface has vertical tractions from water columns, of which heights are locally determined as $(4000 - h(x, z))$ m, where $h(x, z)$ is the topography at a location, (x, z) . The bottom surface is supported by the Winkler foundation. Temperature is fixed at 0 °C on the top surface and at 1300 °C on the bottom surface. We adopt the power-law rheology of dry diabase [e.g., Kirby and Kronenberg, 1987, Buck et al., 2005].

For detail model parameters, please refer to Table 1.

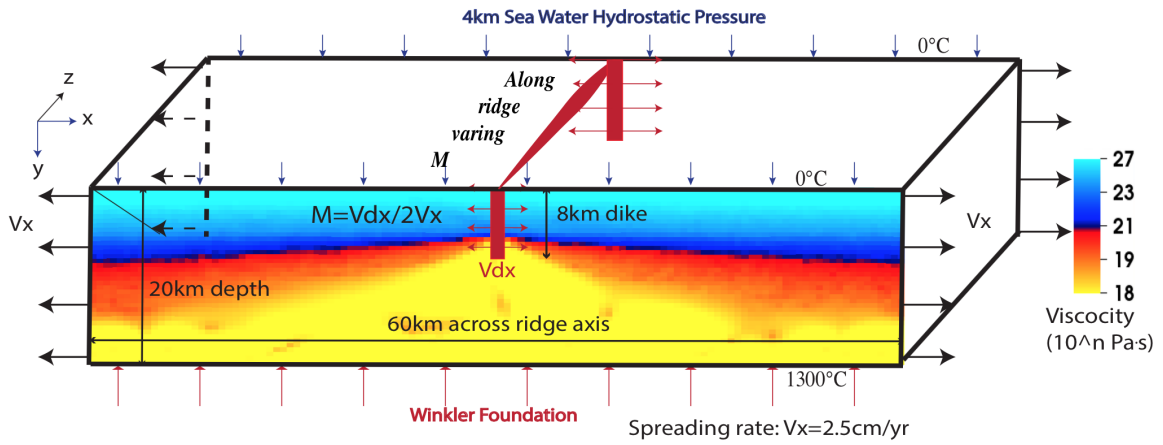


Figure 7: Model setup

2.3 Parameters to control

Before running 3D models, I have run hundreds of pseudo-2D models for initial setup and benchmarking with previous studies [e.g., Buck et al., 2005, Tucholke et al., 2008]. Preliminary pseudo-2D results show that the model behavior in faulting pattern is sensitive to the rate of strain weakening. Two cases of strain weakening are tested in the 3D models. In one case (denoted as Type 1 weakening), cohesion linearly decreases from 44 MPa (denoted as C_i) to 4 MPa (C_e) for plastic strain accumulating from 0 ($\varepsilon_{p_i}^1$) to 0.1 ($\varepsilon_{p_e}^1$). It has a characteristic fault slip of 150 m for pseudo-2D models and 300 m for 3D models. The other case (Type 2 weakening) assumes cohesion linearly decreasing from

44 MPa (C_i) to 4 MPa (C_e) for plastic strain accumulating from 0 ($\varepsilon_{p_i}^2$) to 0.33 ($\varepsilon_{p_e}^2$). In this case, the characteristic fault slip for pseudo-2D models is 500 m and for 3D models is 1 km. The characteristic fault slip is defined as $\Delta X_c = 3\Delta x \varepsilon_{p_e}$ where $3\Delta x$ represents the thickness of the shear bands which is usually 2 to 4 times Δx (size of a hexahedron element) [Lavier et al., 2000]. When ΔX_c amount of slip takes place at the fault interface, the cohesion of the material at the faulting interface decreases to C_e . In this way, under the same amount of ΔX_c , models with different resolution should produce the same faulting patterns.

Meanwhile, although how to estimate the M values from observations is a subject of on-going research, we do have constraints from a large dataset of bathymetry, gravity and seismic surveys as well as geological drilling. Generally, at slow spreading ridges, magma supplies mostly at the center of the ridge segment and decreases towards the tip of the segment [Tolstoy et al., 1993, Chen and Lin, 1999, Carbotte et al., 2015]. There is also evidence for shorter wavelength of 10 to 20 km discrete focus of magma accretion along the ridge axis [Lin et al., 1990]. Based on these constraints, I start considering a few scenarios of variations in M along the ridge axis. They are three M ranges (i.e. 0.2~0.8 (M28), 0.5~0.7 (M57) and 0.5~0.8 (M58)) with three simple functional forms of M variations (i.e. linear, sinusoidal and square root).

The numerical cost of a 3D model is non-trivial. For 2 Myr of model time, each model usually runs on 192 cores for about 48 hours (i.e., around 10^4 core-hours). Under this constraint of computational cost, I control only the following three parameters while fixing all the others: 1) three types of functional forms (i.e. linear, sinusoidal and square root); 2) three ranges of M variation along the ridge axis (0.5~0.7 (M57); 0.5~0.8 (M58); 0.2~0.8 (M28)) and 3) two types of weakening rate (Type 1 and Type 2).

Till now, $11 + 1$ 3D models are run (11 models with M varying along the ridge-axis and 1 model with constant M = 0.8. The complete list of 3D models is given in Table 2.

Table 1: Summary of 3D Model Parameters

Number	Variable	Description	Value	Units
1	W_{dike}	Dike width	2	km
2	D_{dike}	Dike depth	8	km
3	H	Crustal thickness at dike	6	km
4	dT/dy	Crustal thermal gradient	40	K/km
5	T_1	Temperature at lower boundary of crust	240	°C
6	g	Gravity acceleration	10	m/s ²
7	$demf$	Dimensionless force damping factor	0.8	N/A
8	dt	Time step	1.5768e+07	second
9	$topokappa$	Parameter for topography smoothing	0	N/A
10	$shadowDepth$	Ghost elements for parallel computing	2	N/A
11	$meshI$	Mesh number in X direction	60	N/A
12	$meshJ$	Mesh number in Y direction	20	N/A
13	$meshK$	Mesh number in Z direction	20	N/A
14	L_I	Length in X direction	20	km
15	L_J	Length in Y direction	20	km
16	L_K	Length in Z direction	20	km
17	ρ	Density	3000	kg/m ³
18	λ	Lamé's constant	30	Gpa
19	μ	Shear modulus	30	Gpa
20	$refvisc$	Reference viscosity	0.125e-17	Pa ⁻ⁿ /s
21	$activationE$	Activation Energy	276.0e+3	kJ/mol
22	vis_{min}	viscosity minimum cutoff	1.0e+18	Pa * s
23	vis_{max}	viscosity maximum cutoff	1.0e+27	Pa * s
24	$srexponent$	Power of power law in viscosity	3.05	N/A
25	$\varepsilon_{p_i}^1$	initial plastic strain for piecewise Type 1 weakening	0	N/A
26	$\varepsilon_{p_i}^2$	initial plastic strain for piecewise Type 2 weakening	0	N/A
27	$\varepsilon_{p_e}^1$	end plastic strain for piecewise Type 1 weakening	0.1	N/A
28	$\varepsilon_{p_e}^2$	end plastic strain for piecewise Type 2 weakening	0.33	N/A
29	C_i	initial Cohesion for piecewise weakening	44	Mpa
30	C_e	end Cohesion for piecewise weakening	4	Mpa
31	ϕ	Friction angle	30	°
32	$remesh_{timestep}$	Remesh when timestep reach its value	400000	N/A
33	$remesh_{length}$	Remesh when the global minimum of the ratio of the volume of a tetrahedron to one of its surface area	0.6	N/A
34	$topTemp$	Surface temperature	0	°C
35	$bottomTemp$	Bottom temperature	1300	°C
36	V_x	Half spreading rate	7.9e-10	m/s

Table 2: List of 3D numerical experiments.

Model	M range	Functional Form	Type of weakening	For short
1	M28	Linear	Type 1	M28LinT1
2	M28	Sinusoidal	Type 1	M28SinT1
3	M28	Square Root	Type 1	M28SqrtT1
4	M57	Linear	Type 1	M57LinT1
5	M57	Sinusoidal	Type 1	M57SinT1
6	M57	Sinusoidal	Type 2	M57SinT2
7	M57	Square Root	Type 2	M57SqrtT2
8	M58	Sinusoidal	Type 1	M58SinT1
9	M58	Sinusoidal	Type 2	M58SinT2
10	M58	Square Root	Type 1	M58SqrtT1
11	M58	Square Root	Type 2	M58SqrtT2
12	M88	Constant	Type 2	M88ConT2

3 Results

In this “Results” chapter, I first walk through the reference model (M28LinT1) and compare it with a constant M model (M88ConT2). Then, I describe in detail the major characteristics of the models. Finally, I compare the models in terms of 1) two types of the weakening rates; 2) three types of the ranges of M variation and 3) three types of the functional forms of M variation.

3.1 Reference model M28LinT1

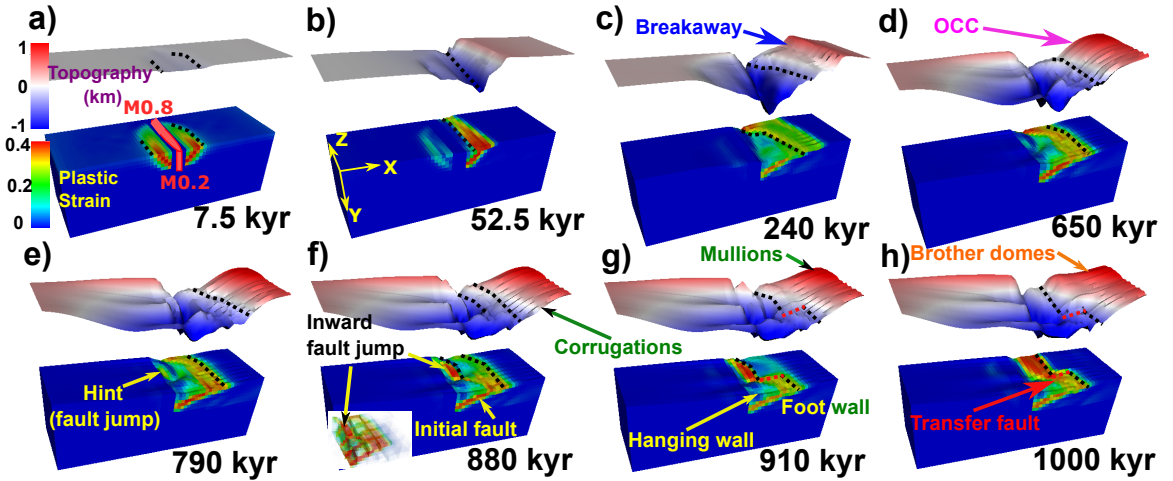


Figure 8: Evolution of plastic strain and surface topography of the reference model M28LinT1 (Table 2). Each snapshot shows plastic strain plotted on the model domain and the five times exaggerated topography. Initial seafloor is marked as a reference of 0 km of the topography. The bold dash lines (black) are the terminations of the detachment faults. The bold dash lines (red) in g and h are the transfer faults that connect the terminations along the ridge. The inset in f plots plastic strain with opacity linearly proportional to its value.

I consider the model with M varies linearly from 0.2 to 0.8 along the ridge axis with type 1 weakening rate (M28LinT1) as our reference model. The major characteristics of the model are indicated in the Figure 8. They are breakaway (Figure 8.c); oceanic core complex (OCC) (Figure 8.d); terminations of the detachment faults where the active faulting interfaces reache the seafloor (Figure 8.e); new high angle normal faults forming near

the ridge axis, termed as “inward fault jump”; corrugations (Figure 8.f) and mullion structures (Figure 8.g); and the side-by-side “brother domes” (Figure 8.h).

As shown in Figure 8, the model creates a median valley that widens and deepens with increasing plate extension (Figure 8.a.b.c). The rate of its widening and deepening at a specific location along the ridge is inversely proportional to the M value (i.e. rate of local magma supply).

For the first 7.5 kyr (Figure 8.a), normal faults (represented by localized plastic strain) begin to form near the ridge axis. Because stresses due to plate motions accumulate faster at the lower M side than at the higher M side, faults initiate at the lower M side first and then propagate to the higher M side.

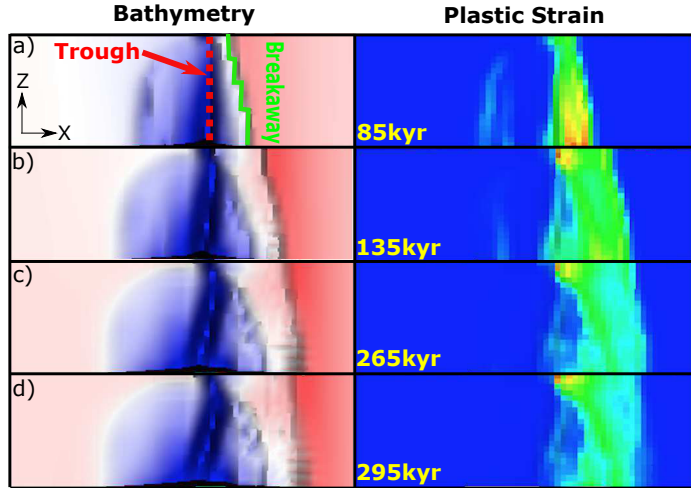


Figure 9: Bird’s-eye view of the evolution of breakaway (marked by green bold line) and depressed narrow zone along the ridge axis (“trough”) (red dash line in (a)) for model M28LinT1 (Table 2). This figure share the same color scales with Figure 8.

By 52.5 kyr (Figure 8.b), the normal fault on the right hand side of the ridge axis continues to evolve while the one on the left becomes inactive. The choice of which fault to develop seems to be made due to a small numerical perturbation between the two faults seen in Figure 8.a although the model setup is symmetrical across the ridge axis. The timing difference of initiation of faulting along the ridge axis creates an offset in the x -axis direction between the breakaways along the ridge that the breakaway at the lower M side

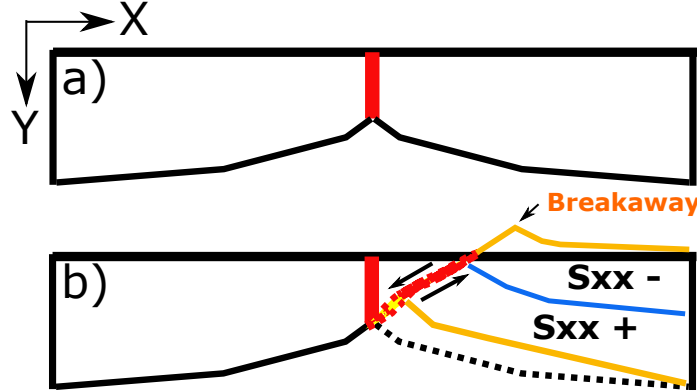


Figure 10: Bending stress illustration. The blue line is the neutral plane where $\sigma_{xx} = 0$. Above the neutral plane is compression ($\sigma_{xx} < 0$) and beneath it is tension ($\sigma_{xx} > 0$).

extends further than that of the higher M side (Figure 9). The offset is maintained because the extending velocity of the breakaways to move away from the ridge axis is controlled by the far field extension rate, V_x . The plastic strain also shows similar along ridge offset in x -axis direction. However, the along ridge offset in x -direction of the tips of the extending plastic strain reduces at ~ 295 kyr (Figure 9.d) because once the detachment fault at the lower M side bends to its lowest dip angle, the termination of the detachment fault stops extending and the healing effect implemented in the model reduces quickly the plastic strain of the inactive fault interface that has been exhumed to the seafloor. While at the higher M side, the termination keeps extending and reduces the initial offset generated by the asynchronous initiation of faulting. In addition, as the fault slips, crust at the footwall bends in a clockwise rotation as illustrated by Figure 10.

By 240 kyr (Figure 8.c), the median valley further deepens and widens. The detachment fault keeps slipping and as it bends, the termination at the lower M side ($M < 0.3$) extends ~ 15 km away from the ridge axis with the dip angle decreases to $\sim 30^\circ$ at the root of the fault and to $\sim 0^\circ$ at the exposed fault interface. However, for the detachment at the higher M side (especially for $M > 0.7$), the dip angle remains high and the termination of the detachment is closer to the ridge axis. The maximum relief between the breakaway and the depressed narrow zone (trough) inside the median valley becomes larger than 1 km. In addition, ~ 1 km wavelength corrugations begin to show up between the break-

away and termination at the lower M side ($M < 0.3$). The wavelength of the corrugations is relatively more regular than the mullion structures (Figure 8.g) because they share different formation mechanism as will be described in the following sections. The trough evolves from a straight line parallel to the ridge axis (Figure 9.a) to a line oblique to the ridge axis and the obliquity increases with extension (Figure 9.b,c,d).

By 650 kyr (Figure 8.d), the median valley becomes wider and deeper. The detachment fault reaches its lowest dip angle and its termination stops extending. The break-away already moved out of the model domain. The fault slip is already larger than the thickness of the crust and the upper mantle materials are exhumed to the surface. The previous fault interface bends over and dips away from the ridge axis, producing a cylindrical OCC. A hint of the inward fault jump shows up at the higher M side ($0.5 < M < 0.65$).

By 790 kyr (Figure 8.e), the hint of the inward fault jump evolves and propagates toward the higher M side ($M > 0.5$). However, the initial detachment fault is still active and takes up most of the extension. The distance between the termination of the detachment fault and the ridge axis varies along the ridge that the termination at the lower M side is further away from the ridge axis.

By 880 kyr (Figure 8.f), at the higher M side ($M > 0.5$), the hint of the inward fault jump evolves to a high angle normal fault that cut through the higher M side ($M > 0.5$) and coexists with the initial detachment fault (shown in the inset).

By 910 kyr (Figure 8.g), the inward fault jump takes up all the extension at the higher M side ($M > 0.5$) and substitutes the initial detachment fault. At the higher M side, previous hanging wall becomes footwall and moves with the spreading plate to the positive x -axis direction, however, at the lower M side, due to the limited magma supply, the hanging wall follows the conjugate plate and moves toward the negative x -axis direction (Figure 11). This opposite directions of velocities result in a dextral shear stress σ_{xz} region at the lower M side ($M < 0.5$) $\sim 45^\circ$ oblique to the ridge axis (Figure 12) and the shear stress zone produces a new trough inside the median valley that aligns with it. Combined

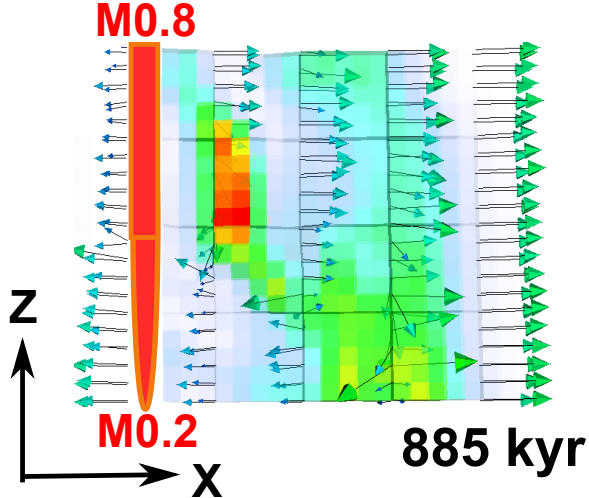


Figure 11: Bird's-eye view of velocity field with plastic strain plotted with opacity linearly proportional to its value. (color scale the same as Figure 8.a))

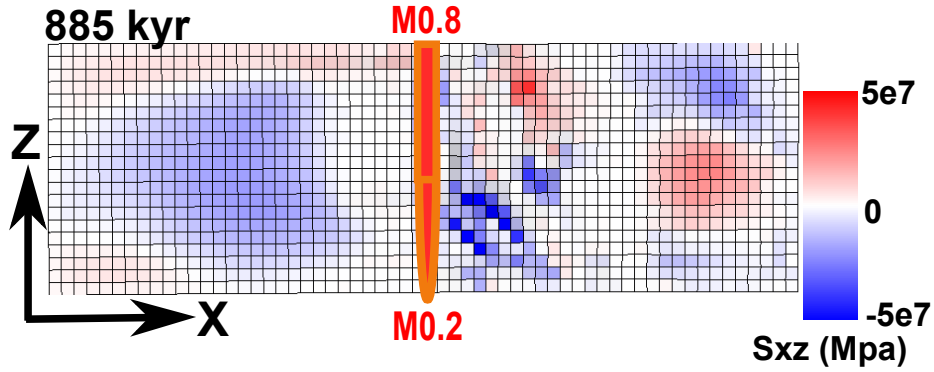


Figure 12: Bird's-eye view of σ_{xz} .

with the previous trough, an “X” shape topography low is created in the model.

3.1.1 Constant M along the ridge axis (M88ConT2 Table 2)

As a comparison to the varying M models, a constant M model is run.

As shown in Figure 13, model M88ConT2 produces a ~ 20 km wide and $1\sim 2$ km deep median valley. It is similar to the generally observation of the Mid-Atlantic Ridges. The width and depth of the median valley is almost constant along the ridge as contrast to the varying M models. The variations of the location of the breakaway and termination along the ridge that mentioned in the reference model (M28LinT1) are not produced. Because the magma supply is constant along the ridge with $M = 0.8$, there is no along ridge

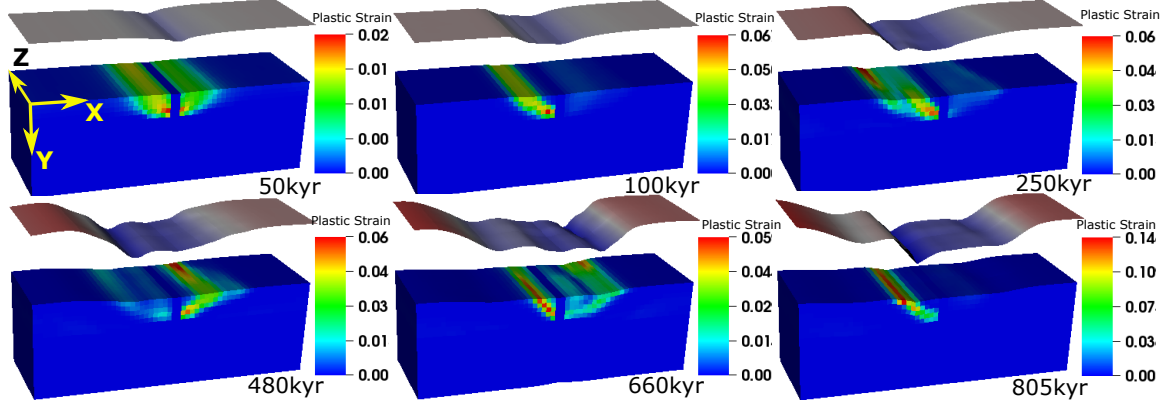


Figure 13: Evolution of plastic strain and surface topography of the model: M88ConT2 (Table 2).

axis variation in the rate of tensional stress accumulation. Thus, the normal faults along the ridge initiate at the same time and the slipping rate of the fault is also constant along the ridge axis. The synchronized fault initiation results in no offset between breakaways and the constant slipping rate produces no along ridge axis variation in the position of the termination. In addition, neither corrugations nor mullion structures are generated. Normal faults alternate on each side of the ridge axis with a period of ~ 300 kyr due to the mechanism mentioned in the “Introduction” section for the 2D models of $M > 0.5$. This fault alternation produces the symmetrical high frequency abyssal hills. For 3D models, why and how fault alternates on each side of the ridge axis is slightly different than the previous 2D studies. It will be further described in the following section.

3.2 Main characteristics of the models

Six main characteristics of the models are described in this section. They are “location of the termination”, “geometry of the trough”, “inward fault jump”, “fault alternation”, “cut-back” and “corrugations and mullion structures”.

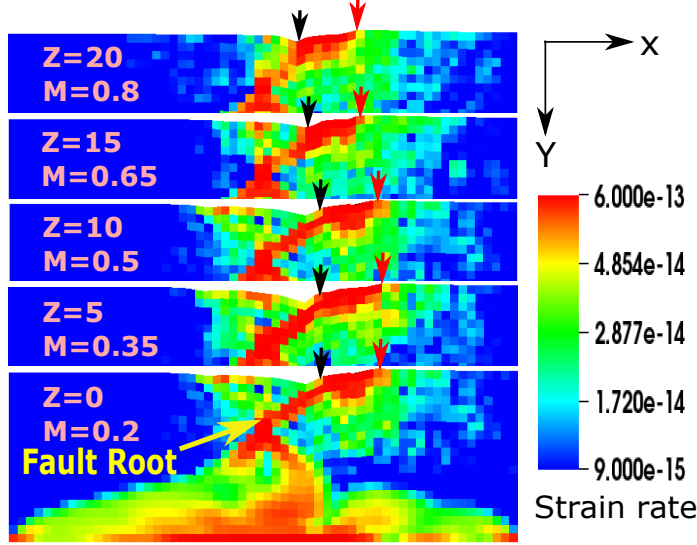


Figure 14: Five slices of strain rate along the ridge for the model M28LinT1 (Table 2) at 107.5 kyr. Terminations and breakaways along the ridge are marked by the black and red arrows respectively.

3.2.1 Location of termination

The location of the termination (bold dash line (black) in Figure 8) of the detachment fault where footwall begins to be exhumed to the seafloor varies along the ridge. As shown in Figure 14, the highest strain rate regions (red) can be interpreted as the active detachment fault interfaces. Compared to the two slices with $M > 0.5$, the distances between terminations and the ridge axis is larger and the dip angles of the detachment faults is smaller at the lower M side ($M \leq 0.5$). For ridge region with $M > 0.5$, fault root is pushed away from the ridge axis due to excessive diking and the termination is closer to the ridge axis due to later initiation of the fault and thus the dip angle is higher because the distance between the termination and the fault root is smaller. For ridge region with $M \leq 0.5$, the distances and the dip angles are similar. Because although the rate of fault slip is higher for lower M , the rotation rate of the detachment fault interface is determined by how fast the termination extends away from the fault root. Since the extending rate of the termination has a maximum value that is restricted by the far field extension rate V_x and the detachment fault roots at the same place at the intersection between the cen-

ter dike and the brittle-ductile transition (BDT), the bending rate of the detachment fault is similar among the three slices of $M \leq 0.5$. One thing needs to be noted is that the trough at the higher M side correspond to the terminations but detached from the terminations at the low M side ($M < 0.5$) as shown in Figure 14.

3.2.2 Geometry of the trough

The depressed narrow region inside the median valley is termed as “trough”. It evolves from a straight line parallel to the ridge-axis (Figure 9.a) to a line oblique to the ridge-axis (Figure 9.b,c,d) for model M28LinT1. Initially, the trough corresponds to the termination of the detachment fault. Due to the coupling along the ridge axis, fault propagates from front to back in almost a straight line parallel to the ridge axis. However, as the detachment fault bends at the lower M side, the trough is detached from the termination and due to lower magma supply, the trough at the lower M side is pulled to the conjugate plate to the negative x -axis direction. While the trough at the higher M side ($M > 0.5$) are pushed away from the ridge axis by the excessive diking. However, since the trough cannot bypass the termination, the trough at $M = 0.8$ is restricted at the termination. Together it generates the curved trough (Figure 9.b,d).

3.2.3 Inward fault jump

The inward fault jump is another common characteristic of the models. As shown in Figure 8, at the region with $M > 0.5$, the existing normal fault is pushed away from the ridge-axis due to excessive diking (Figure 8.c,d). As it moves away from the ridge axis, the frictional energy for the fault, the bending energy for the foot wall as well as the gravity that resists the exhumation of the foot wall increase [Lavier et al., 2000, Olive et al., 2014]. The initial detachment fault remains active until the negative works reach an upper limit that breaking a new fault near the ridge axis needs less work than to maintain the initial one, the initial detachment fault at the higher M side is substituted by the inward jump-

ing fault. This inward jumping behavior of the normal fault is termed as “inward fault jump”. As the fault evolves, it connects to the initial detachment at the lower M side ($M < 0.5$) and generates a curved termination along the ridge. Compared to fault alternation, it forms at the same side of the ridge axis and its length is consistent with the region along the ridge axis where $M > 0.5$ rather than cut through the whole MOR segment.

3.2.4 Fault alternation

As shown in M88ConT2 (Figure 13), the normal fault first evolves on the left hand side of the ridge axis and produces an abyssal hill parallel to the ridge axis. By 480 kyr, another normal fault evolves on the other side of the ridge axis and takes the place of the first one. This behavior of alternatively normal faulting on each side of the ridge axis is termed as “fault alternation”. Among the 12 models (Table 2), only three models produces fault alternation. They are M88ConT2, M58SinT2 and M58SqrtT2. Fault alternates only when weakening rate is low (type 2 weakening) and the average integration of M along the ridge is larger than 0.65. Analysis on when and why fault alternates is given in “Discussion” section.

3.2.5 Cut-back

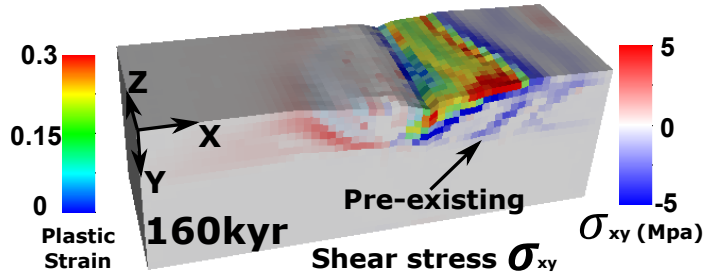


Figure 15: The weak detachment fault tip reaches the pre-existing shear stress at 160 kyr (M28SqrtT1) (Table 2).

Cut-back is another common feature observed in the models. It happens most frequently in the square root models. When the tip of the weak fault interface extends with

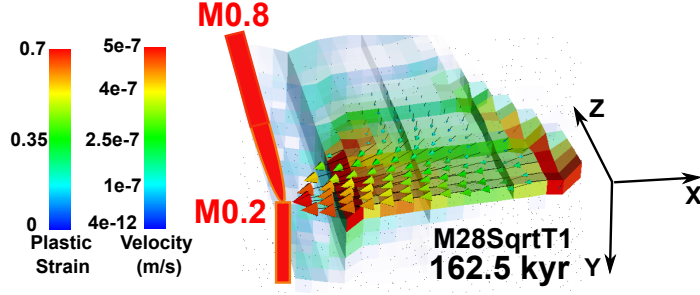


Figure 16: Velocity field of M28SqrtT1 at 162.5 kyr. Magnitudes of the velocity are shown by the colors of the arrow heads. Plastic strain is plotted with opacity linearly to its value.

the plate extension and is intersected by a pre-existing shear stress σ_{xy} (Figure 15), the extra shear stress cuts the tip of the weak fault interface and leads to the decoupling between the spreading plate and the upper layer of the hanging wall of the detachment fault. Under gravity, the decoupled upper layer of the hanging wall then flows backward to the ridge axis with a velocity (Figure 16; Figure 17.b,e (first row)) ~ 10 times faster than the half spreading rate following the topography slope. This behavior is similar to the mass wasting. As the top layer of the hanging wall flows down the topography slope, a sudden topography drop is followed (Figure 17.b) versus c); d) versus e) (topography)). The cut-back also produces a continuous high angle fault scarp with a relief of ~ 1 km aligning to the initial breakaway. The total length of the fault scarp extends for about 20 km along the ridge. The distance between the fault scarp and the central dike varies along the ridge (Figure 17.e (topography)).

Five factors together trigger the cut-back. The unbending force of the bent footwall (Figure 10); the pre-existing shear stress that add extra cutting force to the weak tip (Figure 15); the shear stress that aligns beneath the detachment fault interface that tends to rotate counterclockwise the hanging wall (viewing into positive z -axis direction) (Figure 15); the coupling between the conjugate plate and the hanging wall at the lower M side ($M < 0.5$) that pulls the hanging wall toward the ridge axis; and the asynchronous fault initiation as well as the along ridge variation in the rate of fault slip due to varying

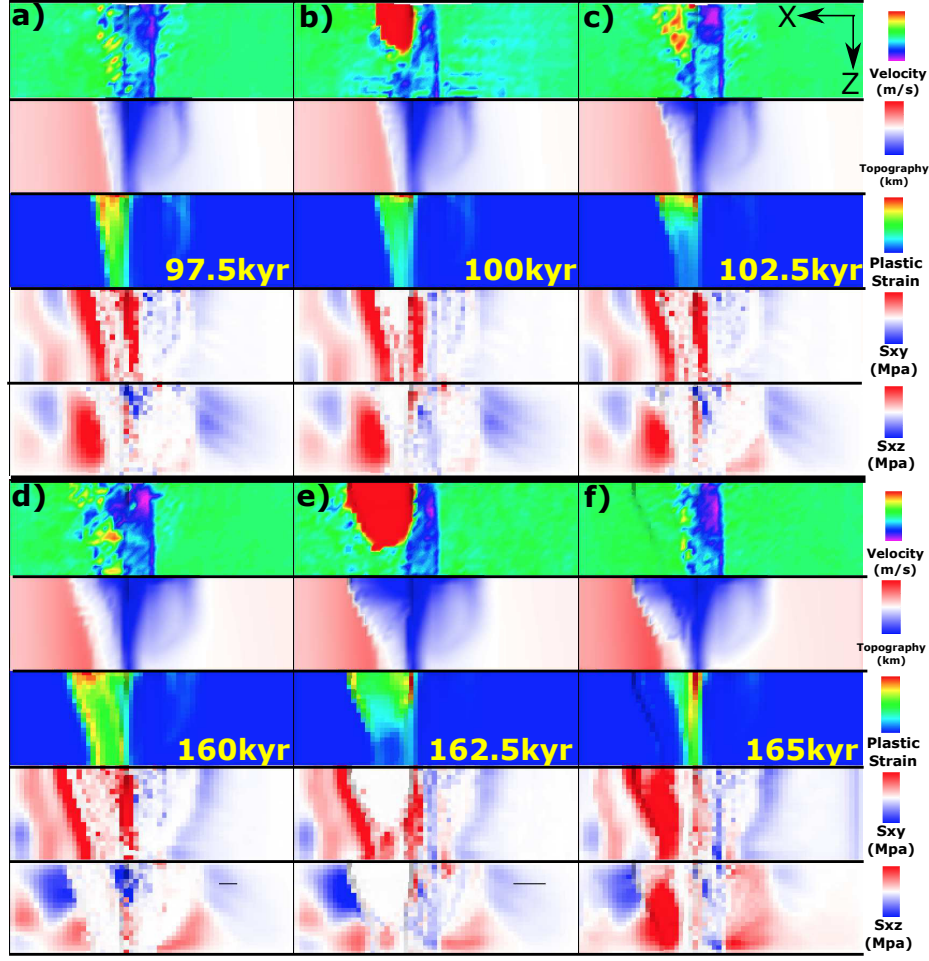


Figure 17: M28SqrtT1 (Table 2). Cut back behaviors in square root functional form model with different time.

M that tend to synchronize the faulting along the ridge and resists the faster extension of the termination at the higher M side (Figure 18).

During the cut-back, mass wasting only happens at the lower M side as shown by the red block of Figure 17.b,e (velocity). The tensional stress due to bending is released only at the lower M side ($0.2 < M < 0.57$) (Figure 19.a compared to b), however, at the higher M side, the tensional bending stress keeps increasing due to the far field extension (Figure 19.c compared to d). This behavior assists in the decouple between lower and higher M side hanging walls. Once the cut back happens at 162.5kyr, the σ_{xy} , σ_{xz} and σ_{xx} are released (Figure 17.e (fourth and fifth row: σ_{xy} and σ_{xz})). Then, σ_{xy} and σ_{xz} soon fill in the area between cut-back created fault scarp and the new termination (Figure 17.f (fourth

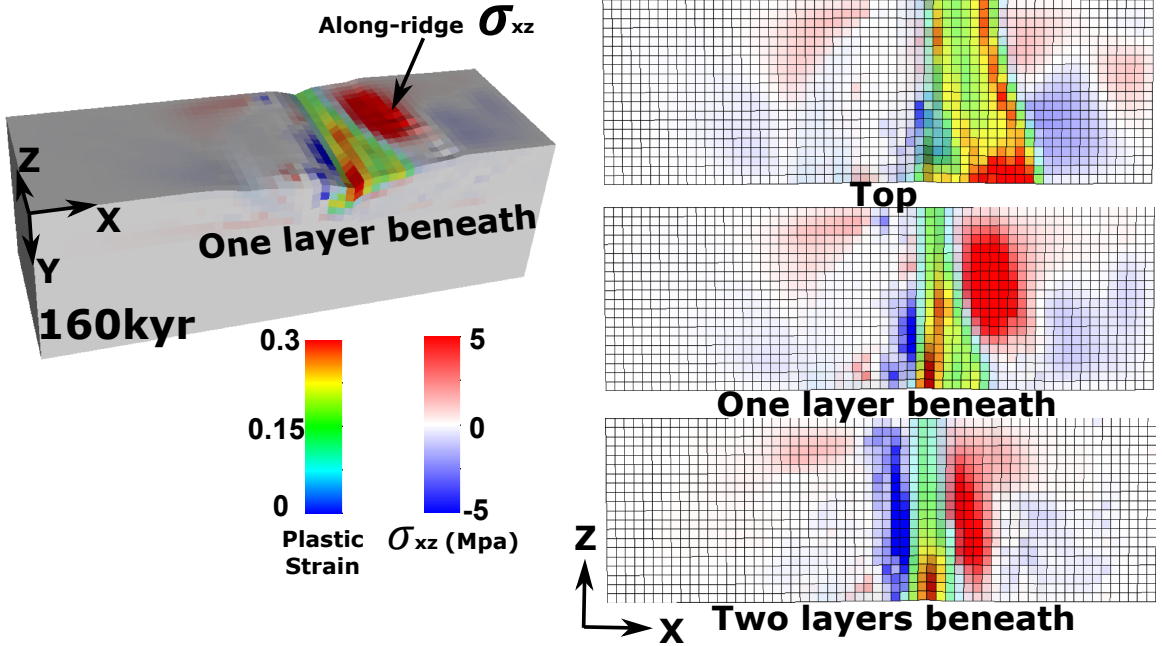


Figure 18: Along ridge axis σ_{xz} (bird's-eye view of three layers of model domain) (positive(red) means clockwise) for M28SqrtT1 at 160 kyr. (Table 2). Plastic strain is plotted with opacity linearly proportional to its value.

and fifth row: σ_{xy} and σ_{xz}).

Immediately after the cut-back, the terminations retreat backward to the ridge axis (Figure 17.d versus f (third row: plastic strain)). This behavior helps maintain a high angle normal fault. Then, the termination at the higher M side extends faster and further than the lower M side (Figure 20). This is partly related to the unbending during the cut-back described earlier that the tensional stress are released at the lower M side but continues to accumulates at the higher M side. Since the tensional stress is released at the lower M side, it takes time to accumulate to the previous stress state and then starts from there to pull the new termination away from the ridge axis. While at the higher M side the increasing tensional stress directly leads to a fast extending termination. This phenomenon is responsible for the corrugations observed. It creates an “X” shape “scan” that first “scan” the topography with faster low M side (Figure 17.d and e) and then “scan” with the faster higher M side (Figure 20.c and d). This results in curved terminations with hundred-to-thousand meters wavelengths that directly create parallel to spreading direc-

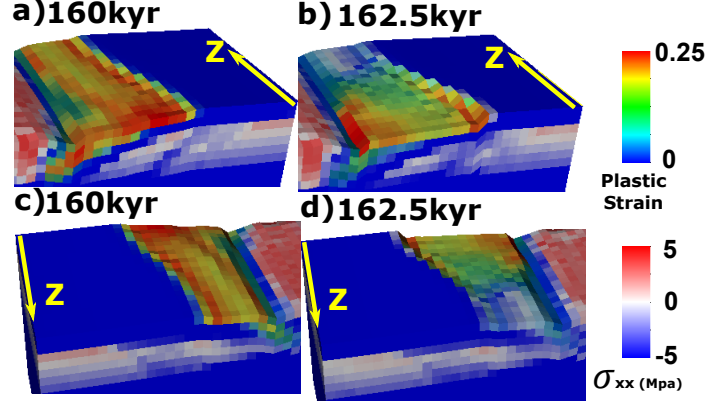


Figure 19: M28SqrtT1 (Table 2). Bending stress drop (a versus b) at the lower M side due to the cut-back. No bending stress drop (c versus d) at the higher M side as a comparison.

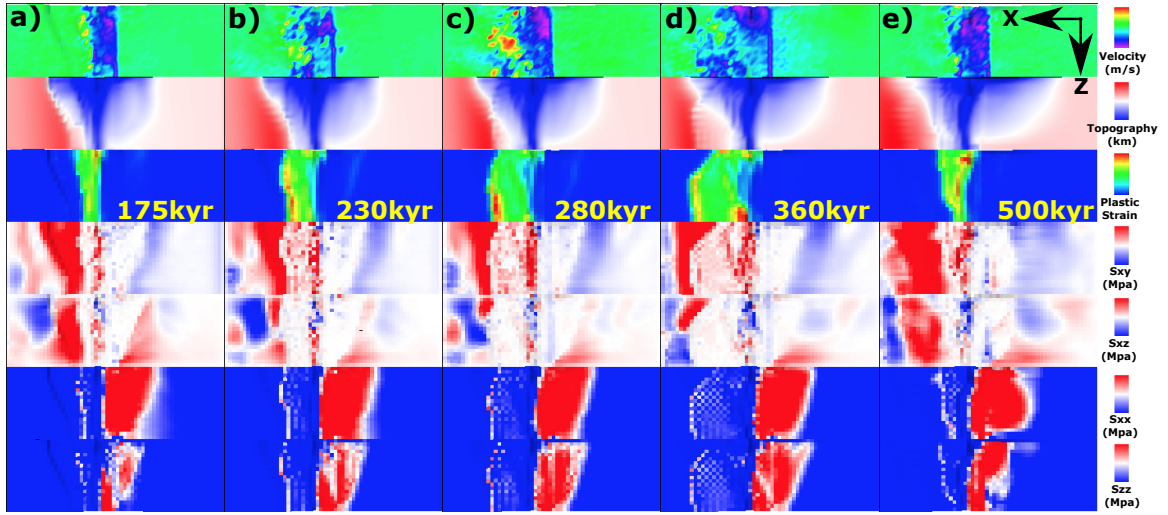


Figure 20: M28SqrtT1 (Table 2). New fault front chase after initial abandoned breakaway.

tion mullion structures.

3.2.6 Hourglass shape median valley

The hourglass shape of the median valley is produced by all the models with varying M along the ridge axis. The shape of the hourglass varies with time. As shown in Figure 21.a, initially, the median valley has similar width along the ridge, however, it has a larger depth at the lower M side because the faults first initiate at the lower M side on both side of the ridge axis and the hanging wall of the faults sink relative to the foot wall. By ~ 100 kyr (Figure 21.b), the fault on the negative x -axis direction of the ridge axis

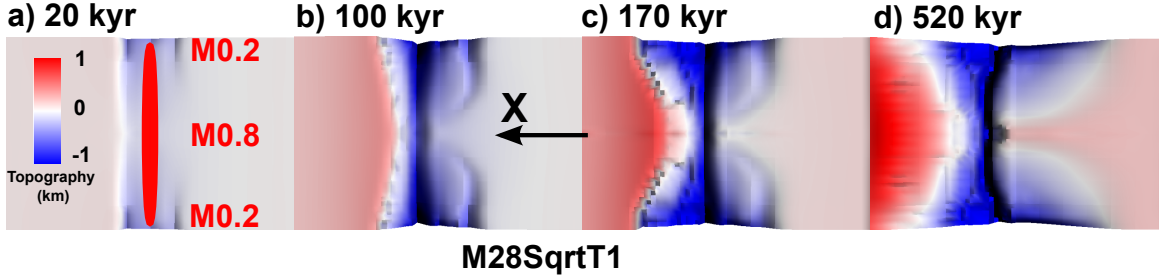


Figure 21: Bird's-eye view of the evolution of the hourglass shape median valley.

doesn't propagate to the higher M side of the ridge and becomes inactive. It produces a curve that is further away from the ridge axis at the lower M side but closer to ridge axis at the higher M side. On the other side of the ridge axis, as the active fault rotates to a lower dip angle, it generates breakaways that are further away from the ridge axis at the lower M side while closer to the ridge axis at the higher M side. This along ridge variation in the location of the breakaways act as another boundary of the hourglass. Both boundaries are extended following the spreading plates. By ~ 170 kyr (Figure 21.c), the hourglass become wider and deeper. Since the area of the cross-section along the ridge inside the hourglass shape median valley is approximately inversely proportional to the local M values, the shape of the hourglass varies with different M variations.

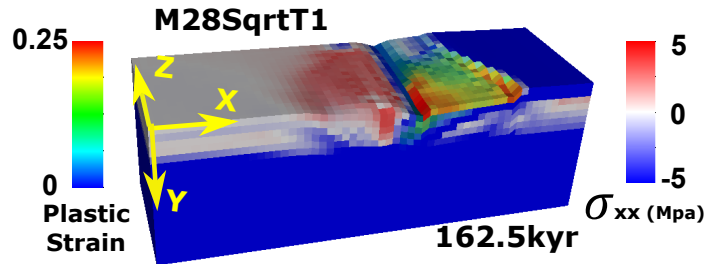


Figure 22: Higher σ_{xx} shows inside the median valley on the negative x -axis direction of the ridge axis.

The further depression inside the median valley on the negative x -axis direction is mostly due to elastic deformation from crustal extension. As shown in Figure 22, the σ_{xx} in the median valley is higher because that the brittle crust is the thinnest at the median valley, when same amount of force propagates from far field extension to the median val-

ley, the stress increases. This increased σ_{xx} is responsible for the further depression and extension of the median valley on the negative x -axis direction of the ridge axis (Figure 21.d). For the median valley on the other side of the ridge axis, cut-back triggered mass wasting between the breakaways and the ridge axis results in the further lowering in topography (Figure 17.d versus e (topography)).

3.2.7 Corrugations and mullion structures

Both corrugations and mullion structures are linear structures parallel to the spreading direction. As shown in Figure 8.f, at the lower M side ($M < 0.5$) on top of the OCC surface, corrugations have a relatively regular undulations with a wavelength of ~ 1 km with hundreds meters in amplitude. While at the higher M side of the ridge (Figure 8.g), the larger mullion structure have a wavelength of ~ 7 km with two other smaller mullion structures on top of its surface. Although corrugations and mullion structures in the models show similar morphologies, they share different formation mechanisms.

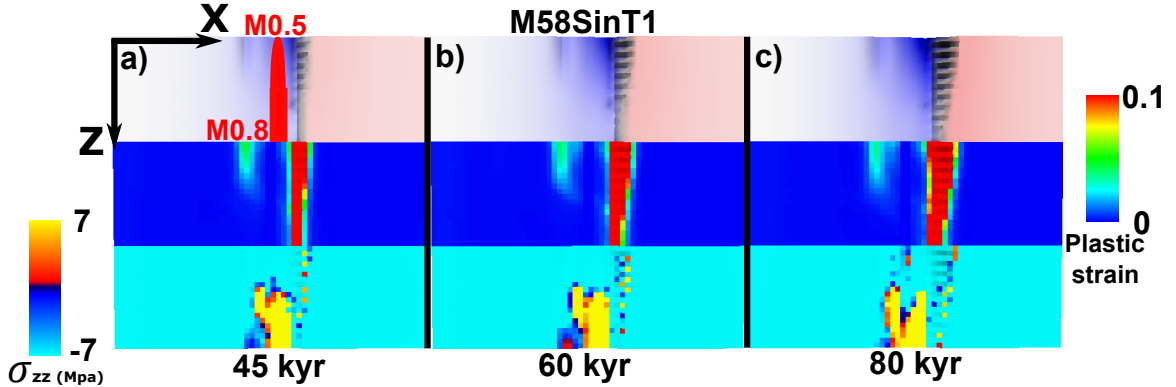


Figure 23: Bird's-eye view of the evolution of the corrugations. Color scales for the topography is the same as Figure 8.

Corrugations

Corrugations are observed in most of the models except for the constant M model M88ContT2 (Figure 13). Among the models that have corrugations, the timing, location and the regularity of the corrugations varies. For example, corrugations in M58SinT1

shows up \sim 45 kyr at the lower M side ($0.5 < M < 0.65$) (Figure 23.a)). However, corrugations in M28LinT1 shows up much later at \sim 240 kyr at the lower M side ($0.2 < M < 0.38$) (Figure 8.c). For M28LinT1, the corrugations are mostly formed at the lower M side ($M < 0.5$) through time and they are less regular along the ridge ((Figure 8.h)). But the corrugations in M58SinT1 appear along the whole ridge and shows regularly alternative undulations with a wavelength of \sim 1 km (Figure 23.c)).

The corrugation is produced at the front tip of the extending plastic strain by tensile failure in the along- z -axis direction. As shown in Figure 23, when the plastic strain reaches or exceeds 0.1 (red color), base on type 1 weakening, the cohesion decreases to 4 Mpa. With a 30° friction angle, tensile failure is declared when the σ_{zz} reaches \sim 7 Mpa (yellow color). The tensile stress results from the asynchronous faulting along the ridge. Since M varies along the ridge, fault initiates earlier at the lower M side of the ridge. Compared to its adjacent higher M side ridge, the foot wall of the fault has a relative displacement that is higher and further away from the ridge axis. This displacement between the foot walls along the ridge generates the isochron-parallel tensional stress σ_{zz} . Since σ_{zz} follows along the extending tip of the plastic strain and as the extending tip of the plastic strain extends, σ_{zz} also extends. Extending tip of the plastic strain together with σ_{zz} generate tensile failure that extends away from the ridge axis and thus produce the linear corrugations that is parallel to the spreading velocity. Detail analysis along with simpler model experiments are given in the “Discussion” section.

Mullion structures

Mullion structures observed in the models are formed by the along ridge variation in the location of the termination due to the evolution of faulting. Mullion structures usually appear at where the termination is closer to the ridge axis. The shape of the foot wall follows the trace of the termination as it is exhumed to the surface. At where the termination is bent inward to the ridge axis, an “initial dome” (Figure 24.a)) is produced once the

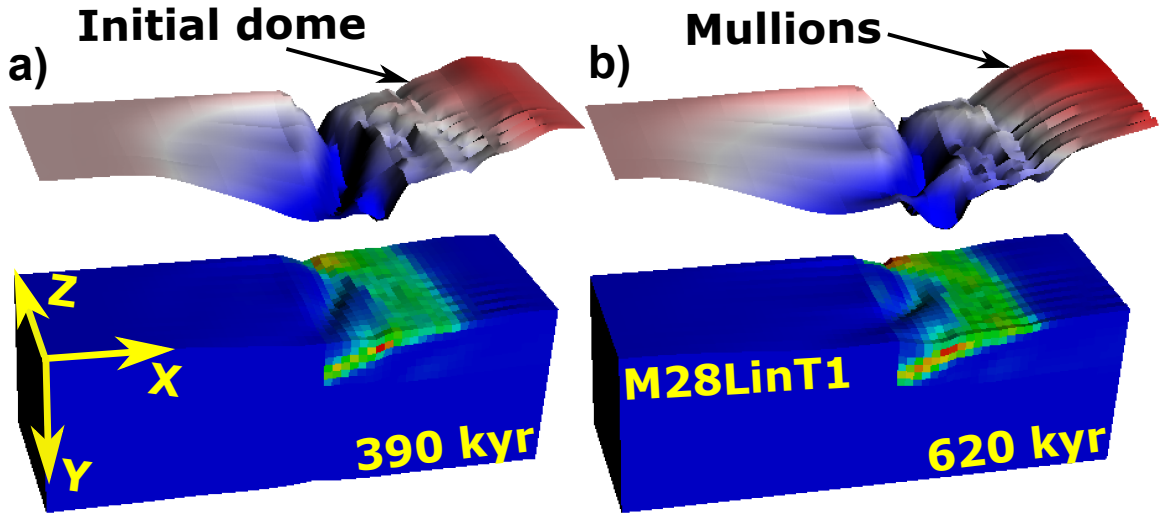


Figure 24: Evolution of mullion structures. Color scales for the topography and the plastic strain are the same as Figure 8.

hanging wall is exhumed to the seafloor. The wavelength of the bulge is determined by the shape of the termination. If the pattern of the termination lasts for a long time and the foot wall of the detachment fault keeps being exhumed to the surface following the trace of the detachment fault termination, a mullion structure is produced (Figure 24.b)).

3.3 Effects of the functional forms of M variation

As shown in the ^{EC:}tables [which table? Specify.], ^{EC:}the models with ^{EC:}M28 [Before starting to use this notation, define and explain it first!] with type 1 weakening is ^{EC:}the only M range that has three functional forms data points available [This sentence gives an impression that you didn't want to use these three but had no choice but to. This is not the case, I believe. Probably you'd want to point out that one of these three is the reference model that has been fully described earlier. So, we are in a better position to compare it with similar models with different functional forms. In fact, I think this introductory sentence can be thrown out.]

^{EC:}There are two phenomena that show distinct differences with respect to different functional forms. By comparing M28LinT1 with M28SinT1 and M28sqrtT1, I identified

two main characteristics in the different behaviors of these models due to different functional forms of M variation. One is the geometry and timing of the secondary fault. The other is the “Cut back” behavior. EC: mostly observed in the square root model. [No need to spill the beans.]

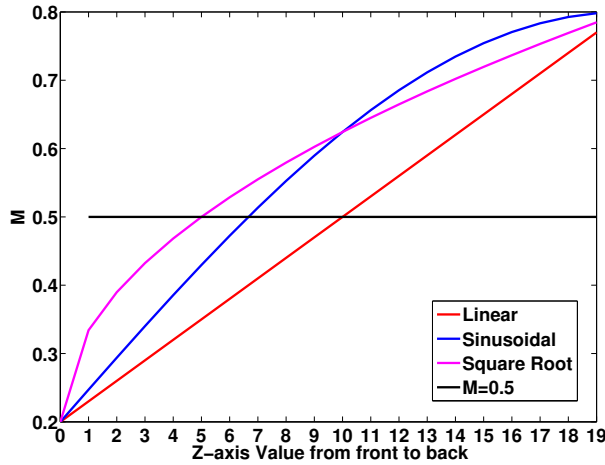


Figure 25: Three functional forms of M variation comparison. They begin to exceed the $M = 0.5$ black line at $Z=10, 7, 5$ for linear, sinusoidal and square root respectively.

Second Fault For the linear functional form, the second fault ^{XT:} [add a definition of secondary fault in the begining, here add a link of figure about primary and sec fault, enlarge the second fault and add label in the figure and use it here] at the high M side has started accommodating most of the extension at around 900 kyr and the initial detachment becomes inactive ^{XT:} [(Figure 26)]refer to Figure 8.f is better. It nucleates from the ridge center where $M = 0.5$ and then propagates to the $M = 0.8$ end.

For the sinusoidal form, the second fault begins to form at a much earlier time around 550 kyr (Figure 26). The sinusoidal form consistently has higher M values than the linear form (Fig. 10), implying a greater amount of magma supply. The first forming fault moves away from the ridge axis faster and locks earlier in the case of the sinusoidal form. As a result, the second fault appears earlier than in the case of the linear M variation. In addition, the sinusoidal form produces the second fault with a greater along-strike dimen-

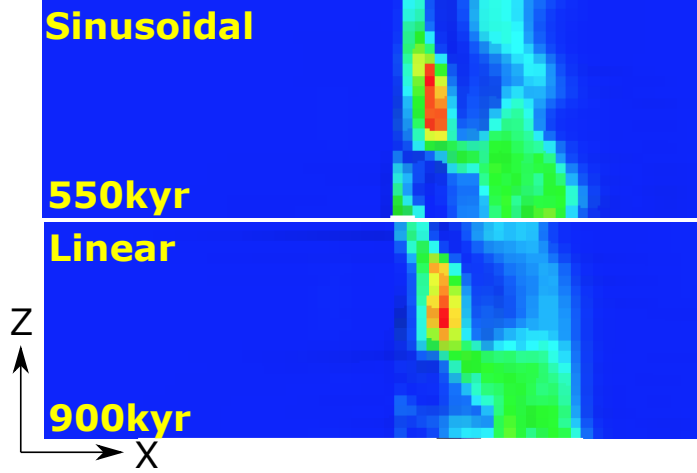


Figure 26: M28LinT1 versus M28SinT1 (Table 2). Secondary fault length comparison between linear and sinusoidal. Around 13 elements in length for sinusoidal compared to 11 elements for linear.

sion than the linear form because this length is proportional to the length of the $M \geq 0.5$ portion of the ridge (Figure 25). For square root, there is no secondary fault forming because the “cut back” behavior releases the tensional stress in the hanging wall.

Cut-back ^{XT:} [Define a cut-back and think about a different name.] The cut-back characterizes but are not limited to the models with the square root form of M variation. ^{XT:} [exclusively about the square root models?] As shown in Figure 27, Figure 28 and Figure 17 ^{XT:} [Bring up Fig. 26 here and include only the cut-back panel.], between 97.5 kyr and 100 kyr, there are cut-backs in the square root model M28SqrtT1 at the low M side where hanging walls with surface area of $\sim 60 \text{ km}^2$ and $\sim 120 \text{ km}^2$ (the red block) suddenly rebound backwards towards the ridge axis as seen in 100 kyr and 160 kyr (Figure 28.a and Figure 17.d,e,f), along with sudden topography drop (Figure 17.d,e 2nd row), σ_{xy} and σ_{xz} released, termination falls back (Figure 17.f 3rd row).

3.4 Effects of the weakening rate

According to our available twelve 3D models, we have three pairs of models that both have type 1 and type 2 ^{XT:} [might want to add a ref to the section defining these.] weak-

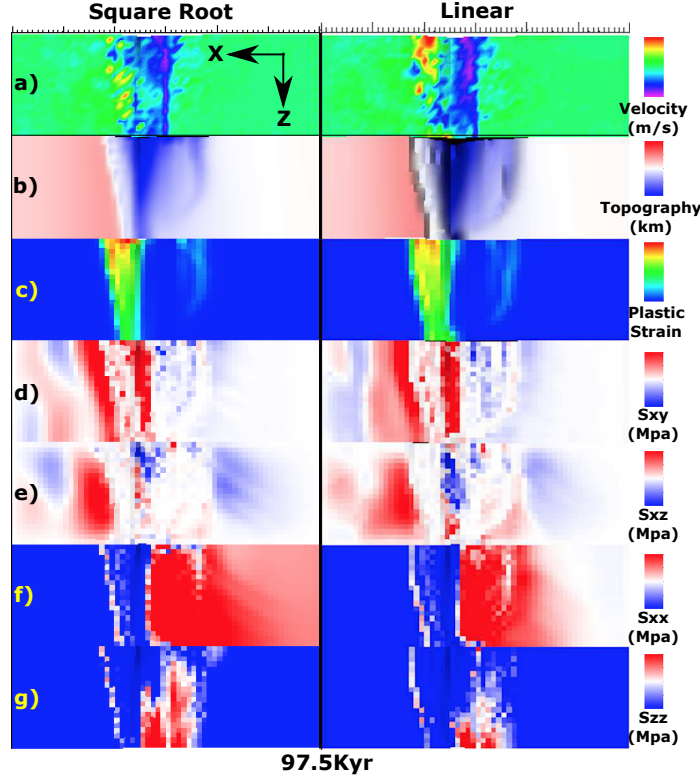


Figure 27: M28LinT1 versus M28SqrtT1 (Table 2) at 97 kyr. View from top of the model.

ening while the range of M and functional form are maintained to be the same. They are M57SinT1/T2, M58SinT1/T2 and M58SqrtT1/T2.

M57SinT1 versus M57SinT2 Initially, both models develop normal faults on both sides of the ridge axis^{XT: [no hyphen in “ridge axis”.]} at the low M side. In the model with the faster weakening rate (M57SinT1), faults propagate toward the high M side and cut through the whole crust by 25 kyr but this process completes later at 50 kyr in the model with the slower weakening rate (M57SinT2). At around 310 kyr, the second fault appears at the high M side^{XT: [instead of z=5, use a M value.]} of M57SinT2 while where $M <= \underline{5}$ [some M value], the initial fault remains active (Figure 29.a) and b)). However, when the weakening is fast (M57SinT1), cut-back happens at around 260 kyr and help to maintain a high angle fault with closer to ridge axis termination. The initial fault remains, no secondary fault forming (Figure 29.a) and b)). In addition, the width of median valley

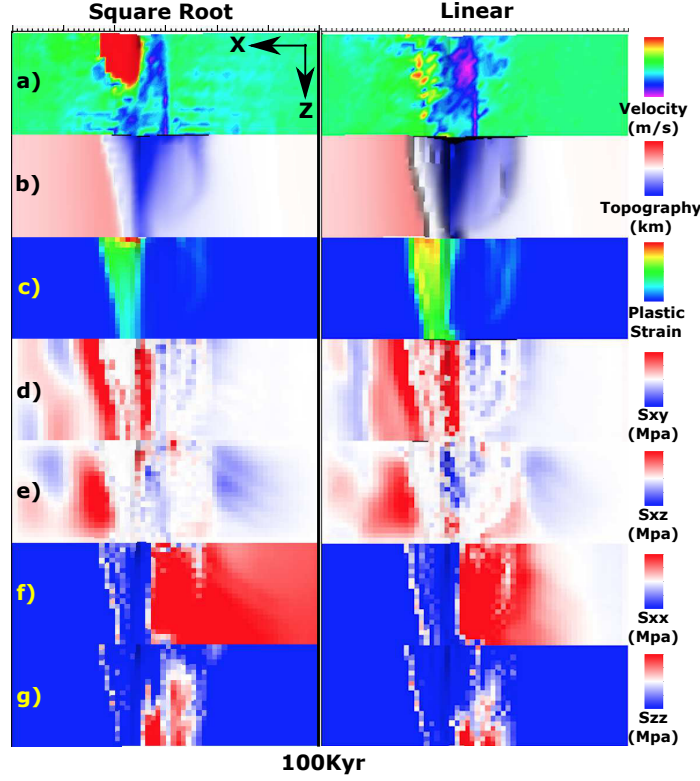


Figure 28: M28LinT1 versus M28SqrtT1 (Table 2) at 100 kyr. View from top of the model.

at low M side is wider for M57SinT2 than M57SinT1 (Figure 29.a) and b) versus c) and d)) due to slower weakening (type 2) allows a more distributed tensional stress σ_{xx} rather than fast weakening that once a fault is established, larger amount of tensional stress σ_{xx} will be released at the fault.

M57SinT1 For M57SinT1, as shown in Figure 30, at 400 kyr (Figure 30.a), there is an antithetic fault forming at the low M side accommodating part of the extension, which results in a curved termination at the far frontier. As it evolves (530 kyr (Figure 30.b)), the termination at the low M side further recedes backward while the termination at the center ($Z = 11 \sim 13$) extends further. This curved termination leads to a curved topography (white curve in the second row). As the fault evolves and bends further away from the axis, at the time of 740 kyr, another antithetic fault forms again at the low M side (Figure 30.c). It doesn't take the place of initial fault and disappear soon, however, it again re-

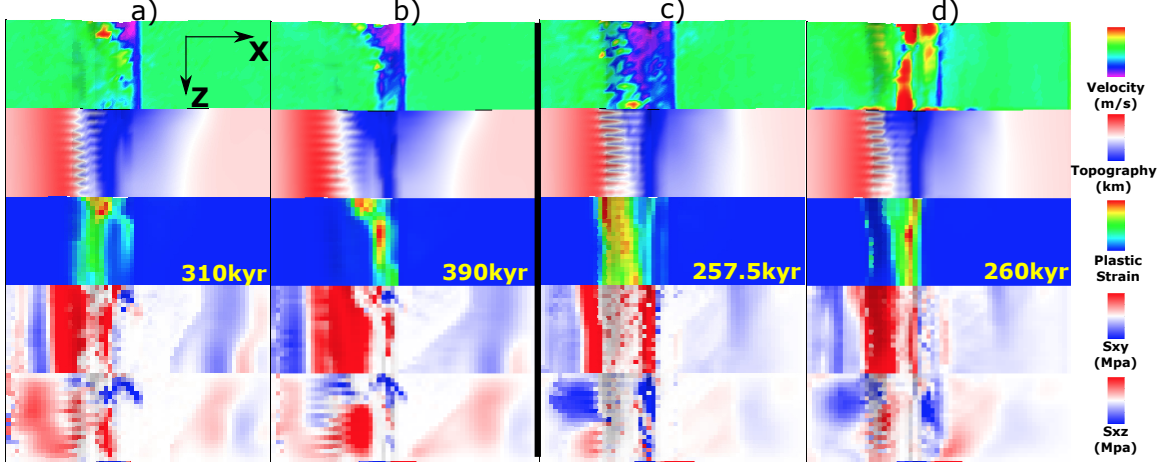


Figure 29: M57SinT2 versus M57SinT1 (Table 2). a) and b) are for M57SinT2, c) and d) are for M57SinT1.

leases tensional stress and results in that the termination at far front recedes backward. At 1000 kyr (Figure 30.d), an Atlantiss Massif shape OCC is produced (low M side (lower magma supply) has a wider dome and high M side (higher magma supply) has a narrower dome) due to the along ridge axis termination evolution. Corrugations with wavelength varying from hundreds to kilometers are also created.

M57SinT2 For M57SinT2, as shown in Figure 31, instead of maintaining one fault all the time for M57SinT1, it creates secondary fault at high M side with different mechanism several times. A secondary fault is created at 325 kyr (Figure 31.a), when a new near axis normal fault take the place of the initial one at high M side. Between 447.5 kyr (Figure 31.b) and 450 kyr (Figure 31.c), termination falls back, and as it evolve, termination at the high M side extends further at 600 kyr (Figure 31.d). At 885 kyr (Figure 31.e), a secondary fault propagates from low Z to high Z and terminates the further extended fault at high Z and maintain a near ridge axis termination.

3.4.1 M58SinT1 versus M58SinT2

A major difference between M58SinT1 and M58SinT2 is that M58SinT1 keep faulting at one side of the ridge axis while M58SinT2's fault alternates.

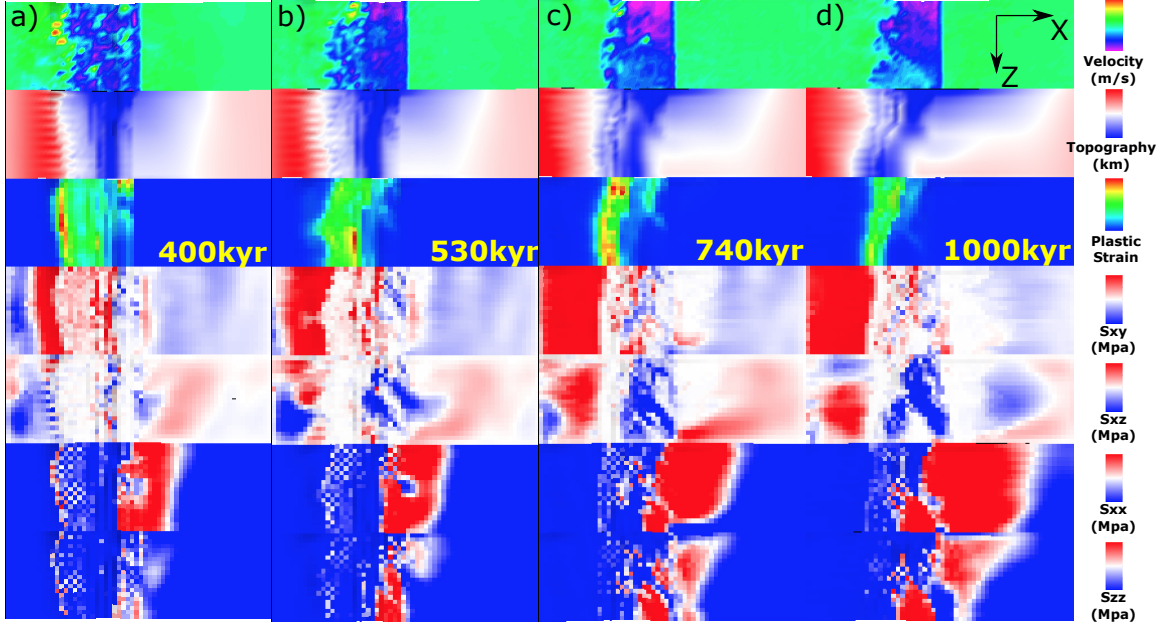


Figure 30: M57SinT1 (Table 2) faulting and stress evolution with respect to time.

M58SinT1 As shown in Figure 32, in 1Myr, the fault keeps on the right hand side of the ridge axis. It evolves dynamically. Between 240 kyr (Figure 32.a) and 245 kyr (Figure 32.b), there is a cut back. At 345 kyr (Figure 32.c), at low Z side, there are two offsetted antithetic faults ($Z=1 \sim 2$ and $Z=5 \sim 9$) in the hanging wall begin to evolve and soon connect to each other forming anastomosing fault zone. At 390 kyr (Figure 32.d), the new near axis anastomosing fault zone replace the old further away from ridge axis detachment. There is dextral σ_{xz} forming on the right hand side of the new anastomosing fault zone ((Figure 32.d), row 5) due to the offset between the new near axis fault at low Z side and extended further fault at high Z side and leads to the development of a $\sim 45^\circ$ shear zone connection between the new near axis fault zone at low Z side and the further away from axis original detachment at high Z side. It also creates a curved termination which will lead to a curved topography (boundary between blue and white) seen at 530 kyr (Figure 32.e). Note that this curved termination can be a mechanism for producing large wavelength (several kilometers) undulating corrugations. Between 530 kyr (Figure 32.e) and 550 kyr (Figure 32.f), there is another cut back happens. Terminations fall

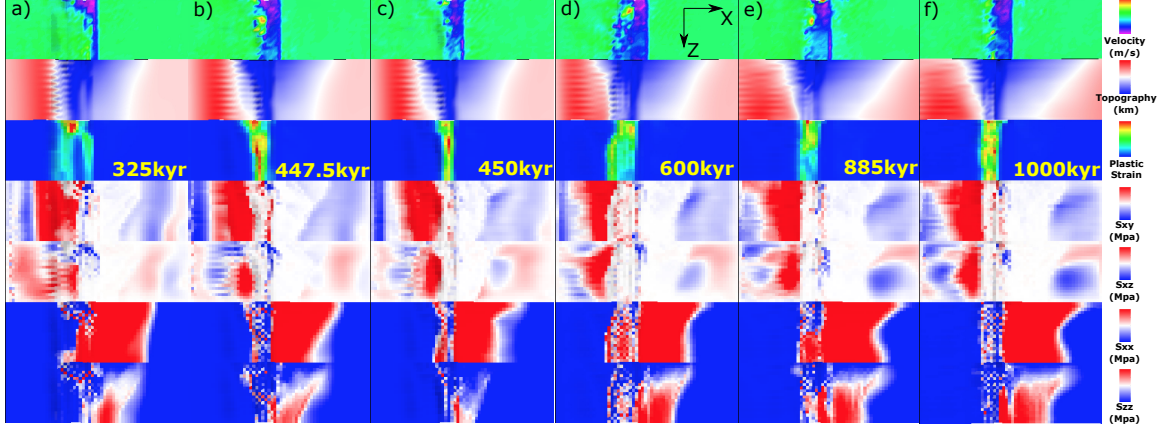


Figure 31: M57SinT2 (Table 2) faulting and stress evolution with respect to time.

backwards to near ridge axis position. At 580 kyr (Figure 32.g), at the high Z side, a new near ridge-axis high angle normal fault begin to initiate under the assistance of rotational force from low Z side due to along ridge axis coupling. This produces a large rider block with several kilometers in its length scale. Previous “S” curved termination now evolves to a half circle curve and it soon affects the curve of topography as seen at 850 kyr (Figure 32.h). Due to along ridge axis variation in diking, a large sinistral shear zone (red region $\sim 40^\circ$ oblique to ridge axis seen in 5th row of 960 kyr (Figure 32.i)) keep developing and cut the circle curved fault zone at 850 kyr (Figure 32.h) into a new fault zone with higher curvature as seen in 1000 kyr (Figure 32.j).

M58SinT2 As shown in Figure 33, the fault initiates on the left hand side of the ridge axis (Figure 33.a). Low Z side extends further than high Z side. It takes around 100 kyr to form into a localized fault plane due to slower rate of weakening. At 215 kyr (Figure 33.b), another fault on the conjugate plate begin to evolve and replaces the initial one. As seen from (Figure 33.b), corrugations are created at low Z side. At 330 kyr, a third fault forming at the left hand side of the ridge axis. Between 490 kyr (Figure 33.d) and 495 kyr (Figure 33.e), there is a cut back.

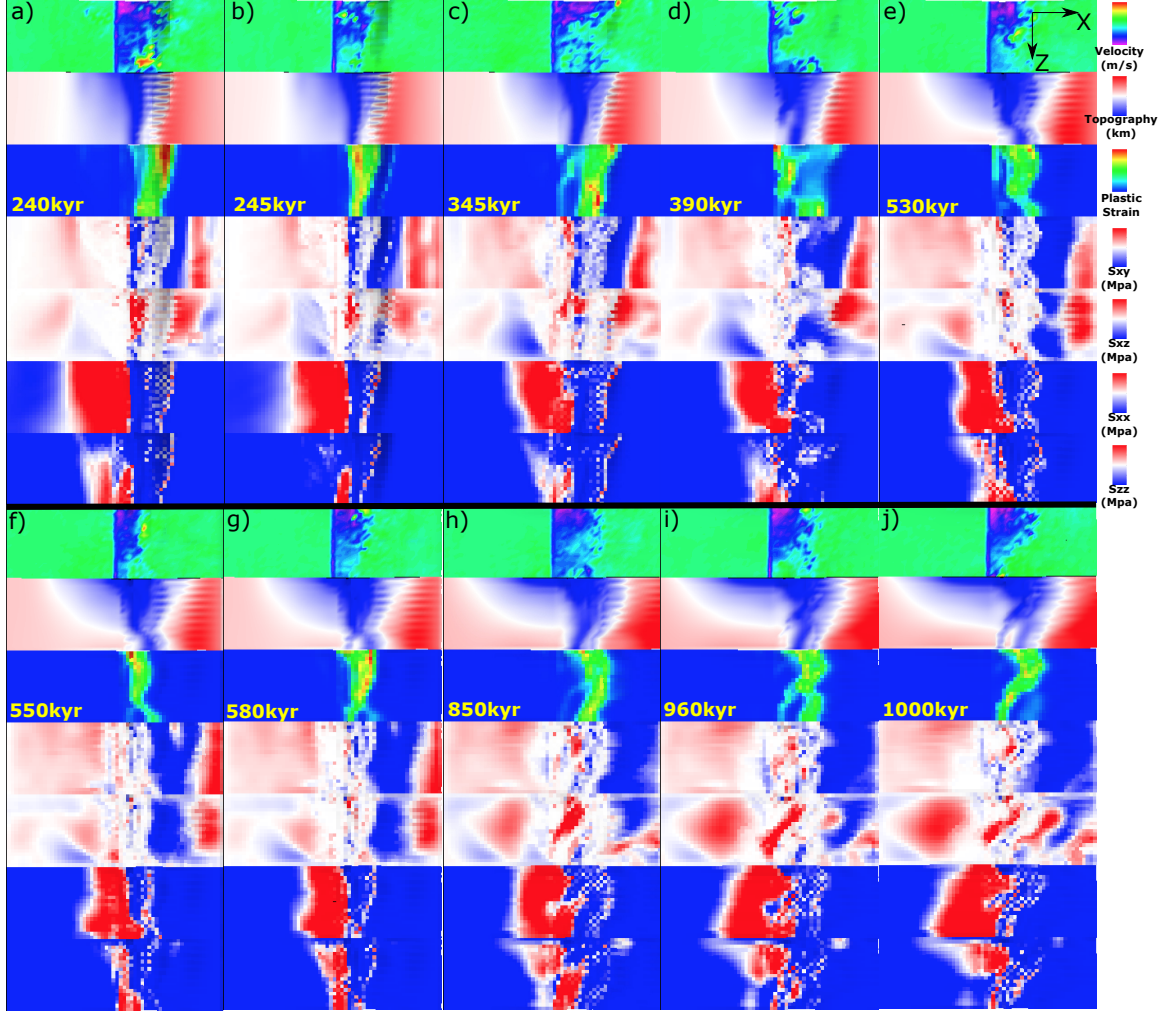


Figure 32: M58SinT1 (Table 2) faulting and stress evolution with respect to time.

3.4.2 M58SqrtT1 versus M58SqrtT2

The major difference between M58SqrtT1 and M58SqrtT2 is also whether the normal fault alternates or not.

M58SqrtT1 As shown in Figure 34, initially, there is a 5 element offset between breakaways along the ridge axis due to along ridge axis variation in diking (Figure 34.a). At 370 kyr (Figure 34.b), there is a vertical tensile failure at $Z = 1 \sim 2$. Two parallel dextral (blue) shear regions are seen (5th row). The low Z shear zone assists in the shear failure observed at 400 kyr (Figure 34.c), and it develops into near ridge axis normal fault

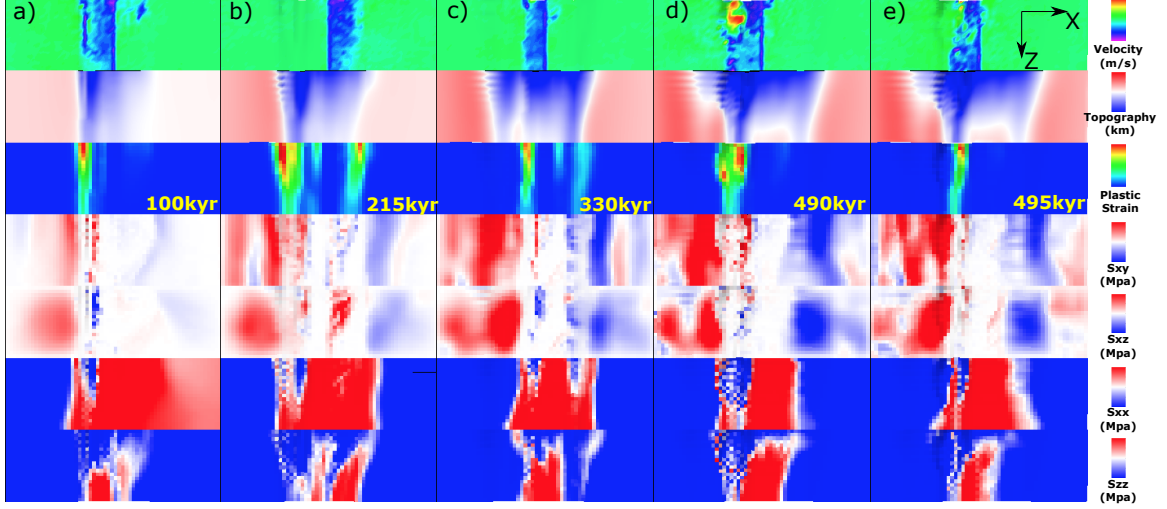


Figure 33: M58SinT2 (Table 2) faulting and stress evolution with respect to time.

($Z=4 \sim 12$) and propagates to high Z side which eventually cuts through and reaches $Z= 20$ and replaces the initial extended fault at high Z side at 460 kyr (Figure 34.d). The vertical tensile failure zone at $Z= 1 \sim 3$ (Figure 34.d 3rd row) begin to evolve and assists in the initiation of a new near ridge axis high angle normal fault which connect with the fault at the high Z side (Figure 34.e) at 590 kyr. At 660 kyr (Figure 34.f 3rd row), there is a hint of high angle normal faulting at $Z= 1 \sim 3$ of conjugate plate. But it doesn't develop. At 730 kyr (Figure 34.g 5th row), a dextral (blue) shear zone at the low Z side help to create the faulting pattern seen at 780 kyr (Figure 34.h 3rd row), a concave termination with a wavelength of 10 kilometers and it has the potential to create a large wavelength corrugation. Meanwhile, at the low Z side, near the ridge axis, there is a antithetic fault forming at the hanging wall of the detachment and it later propagates to high Z side (Figure 34.i). From 820 kyr to 880 kyr, the antithetic fault evolves to near ridge axis normal fault and connects with the detachment at the high Z side (Figure 34.j). In addition, a tensile failure shows its hint at the low Z side ($Z= 1 \sim 5$) of the conjugate plate.

M58SqrtT2 As shown in Figure 35, at 195 kyr (Figure 35.a), due to transtensional stress at low Z side ($Z= 1 \sim 6$), several corrugations begin to evolve. At conjugate plate, dipping toward axis shear zone σ_{xy} (red at 4th row) show its curve and keeps ac-

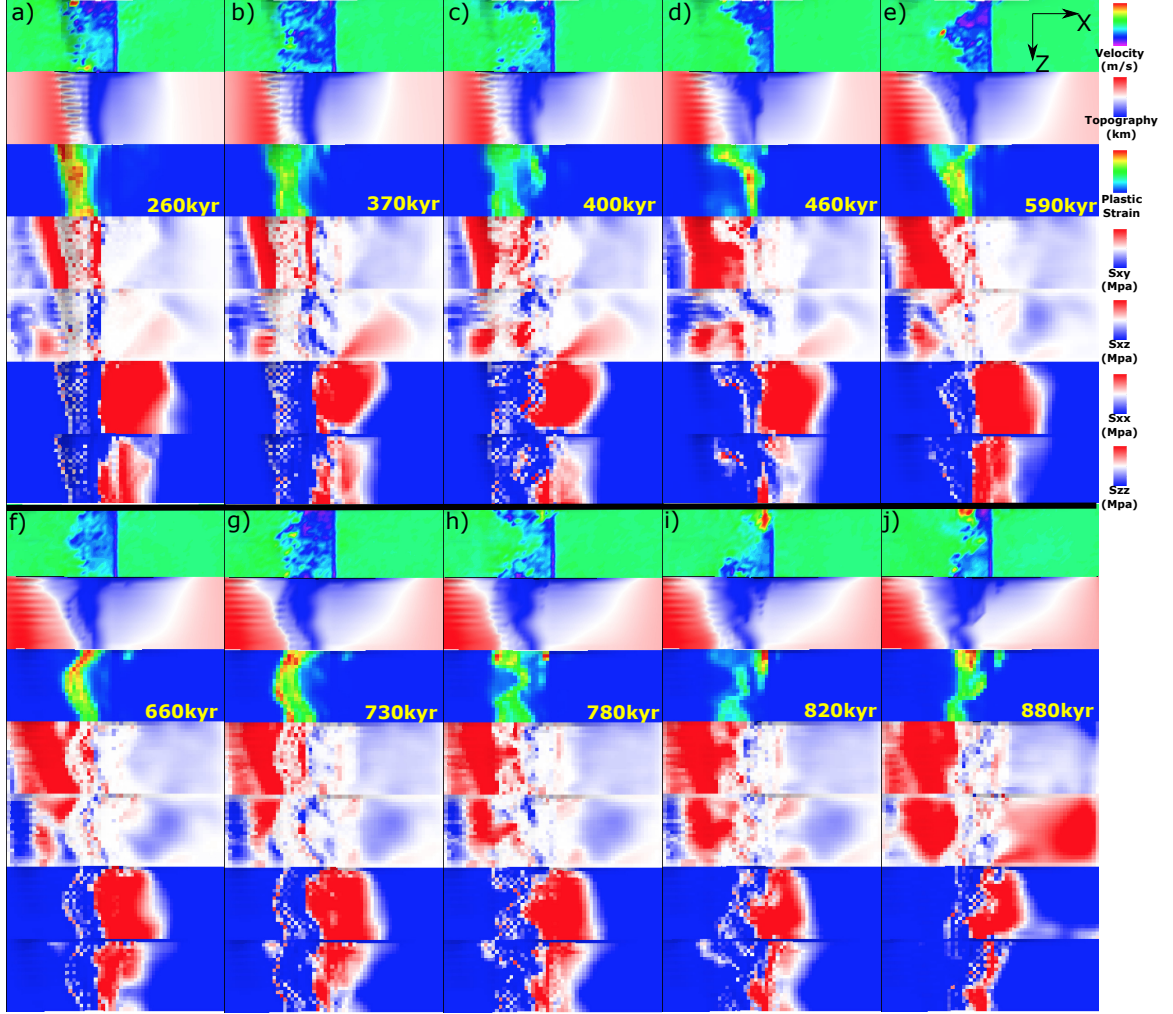


Figure 34: M58SqrtT1 (Table 2) faulting and stress evolution with respect to time.

cumulating. σ_{xx} is also accummulating on the conjugate plate. Between 195 kyr (Figure 35.a) and 200 kyr (Figure 35.b), there is a cut back. At 270 kyr (Figure 35.c), immediately above and following the curved shape shear σ_{xy} zone on the left hand side of the ridge axis, a new fault begin to evolve and replace the initial fault on the right. At 330 kyr (Figure 35.d), at the low Z side, a new near axis high angle normal fault take the place of initial further away from ridge axis fault partly due to rotational force from along ridge coupling. At 460 kyr (Figure 35.e), another normal fault begin to evolve on the right hand side of the ridge axis.

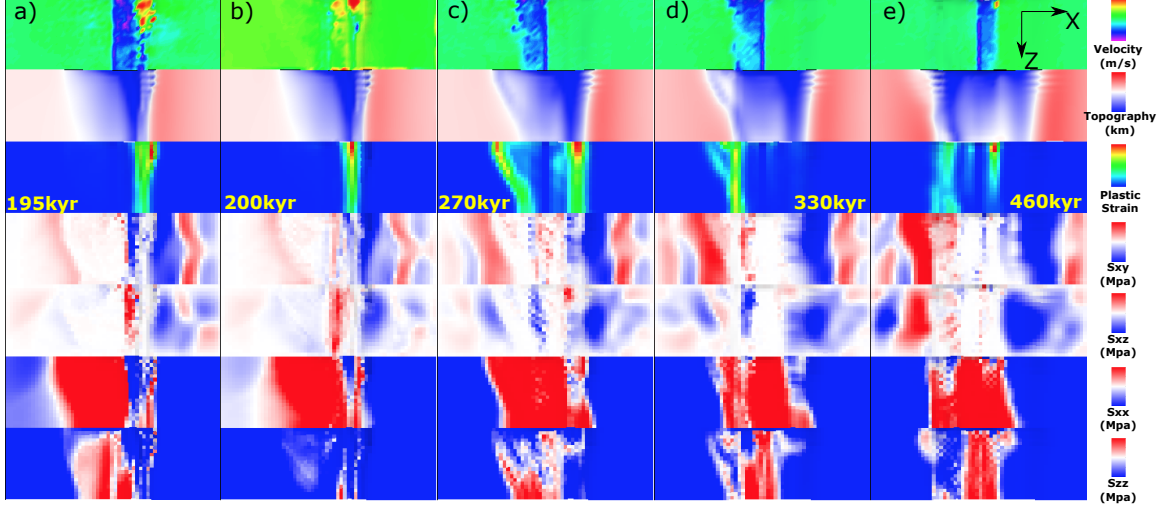


Figure 35: M58SqrtT2 (Table 2) faulting and stress evolution with respect to time.

3.5 Effects of the range of M variation

So far, we have three ranges for M variations along the ridge axis (M28, M57 and M58) with same segment length of 20km. Among the 12 available models, two M58 models and the constant $M = 0.8$ model with type 2 weakening produce fault alternation while others do not. Generally, M57 and M58 models create a median valley much narrower and shallower than that of M28 models. $\frac{dM}{dz}$ is larger for M28 than M58 and M57.

3.5.1 M28SinT1 versus M57SinT1 versus M58SinT1

M57SinT1 versus M58SinT1 For description of M57SinT1 evolution with respect to time, please refer to Section 3 and Figure 30. For description of M58SinT1 evolution with respect to time, please refer to Section 3.4.1 and Figure 32. Comparing M57SinT1 and M58SinT1, the major difference is that the faulting pattern evolution for M58SinT1 is much more dynamic with a higher frequency of secondary faults, cut back and offseted fault segments connection. For M58SinT1, the new secondary near ridge axis normal or antithetic faults usually replace the existed one. However, for M57SinT1, diking is not strong enough to create big enough stress perturbation along the ridge axis for secondary or antithetic faults to take the place of the original one. At the low Z side, near ridge axis

antithetic fault only helps to accommodate tensional stress which help maintain a high angle normal fault with near to ridge axis termination while the termination at the high Z side gradually move off axis. This creates a OCC with larger dome at lower magma supply side than that of higher magma supply side which is opposite to the shape of OCC created by M58SinT1.

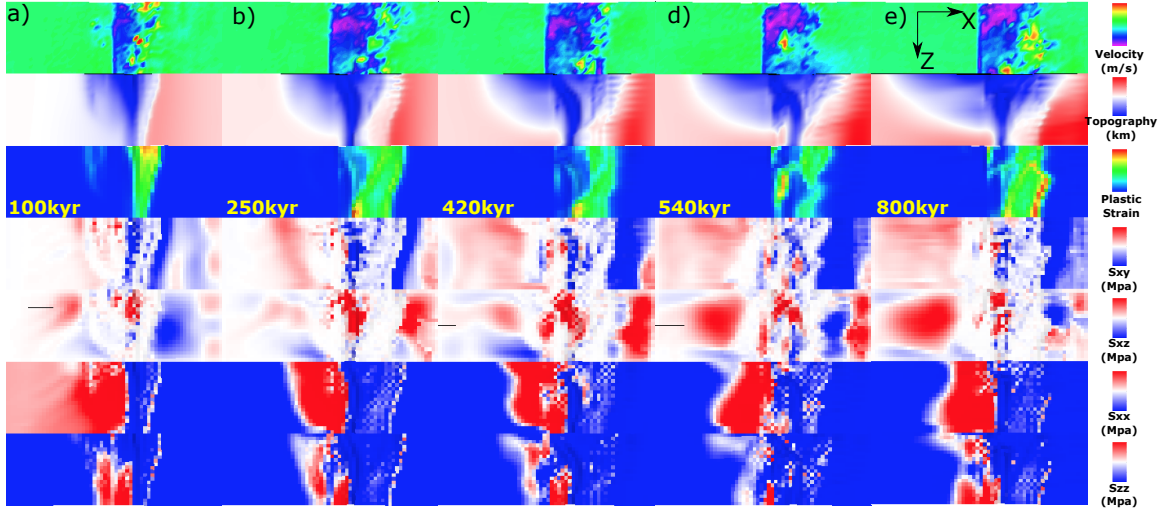


Figure 36: M28SinT1 (Table 2) faulting and stress evolution with respect to time.

M28SinT1 As shown in Figure 36, faulting evolution is much less dynamic than that of M58SinT1. Faulting keeps on the right hand side of the ridge axis. Only one secondary fault is formed at around 540 kyr (Figure 36.d). Initially, at 100 kyr (Figure 36.a), at the low Z side, the normal shear zone at conjugate plate takes up part of the extension and leave a dent in the topography. But it doesn't last long. The initial breakaway of the detachment extends further away from ridge axis with four elements in along ridge axis offset at 250 kyr (Figure 36.b). At 420 kyr, at the high Z side, a hint of new near ridge axis high angle normal fault begin to show up. It develop into a secondary fault at 540 kyr (Figure 36.d) and propagates toward high Z side. This results in a sinistral shear zone (red region in 5th row). At the low Z side ($Z = 1 \sim 3$), a tensile failure can be seen and it take up part of the extension at the low Z side which results in the recede of termination at the low Z side as seen at 800 kyr (Figure 36.e) while the termination at higher Z side extends

further away from the ridge axis.

3.5.2 M57SinT2 versus M58SinT2

For description of M57SinT2 evolution with respect to time, please refer to Section 3 and Figure 31. For description of M58SinT1 evolution with respect to time, please refer to Section 3.4.1 and Figure 33. A major difference is that M57SinT2 does not create alternating normal faults on each side of the ridge axis while M58SinT2 does. ^{XT:}Why this seemingly small change could lead to such a to the first order difference in model behaviors?

3.5.3 M28LinT1 versus M57LinT1

For description of M28LinT1 evolution with respect to time, please refer to Section 3.1.

M57LinT1 As shown in Figure 37, between 160 kyr (Figure 37.a) and 162.5 kyr (Figure 37.b), there is a cut back. The corrugation is very severe and have a discrete distribution with one element width as its wavelength. The frontier of breakaway also shows discrete distribution of σ_{xx} and σ_{zz} alternating between tension and compression which might be the reason for the undulating topography. At 350 kyr (Figure 37.c 3rd row), the two offsetted red line indicates tensile failure at the termination and the shorter one at the high Z side helps maintain a near ridge axis high angle normal fault. At 430 kyr (Figure 37.d), the presence of vertical tensile failure near the ridge axis at the low Z side is responsible for the recede of the front of the plastic strain at $Z= 1 \sim 3$. While at $Z=5 \sim 10$, the breakaway keeps extending further away from the ridge axis. This curved front results in a curved topography as seen in 640 kyr (Figure 37.e) and is also responsible for the large dextral shear (blue) zone (5th row). At 705 kyr (Figure 37.f), a new near ridge axis secondary fault begin to evolve and replace the original one at high Z side with a length of ~ 15 kilometers. The secondary fault also connect with the further away from ridge

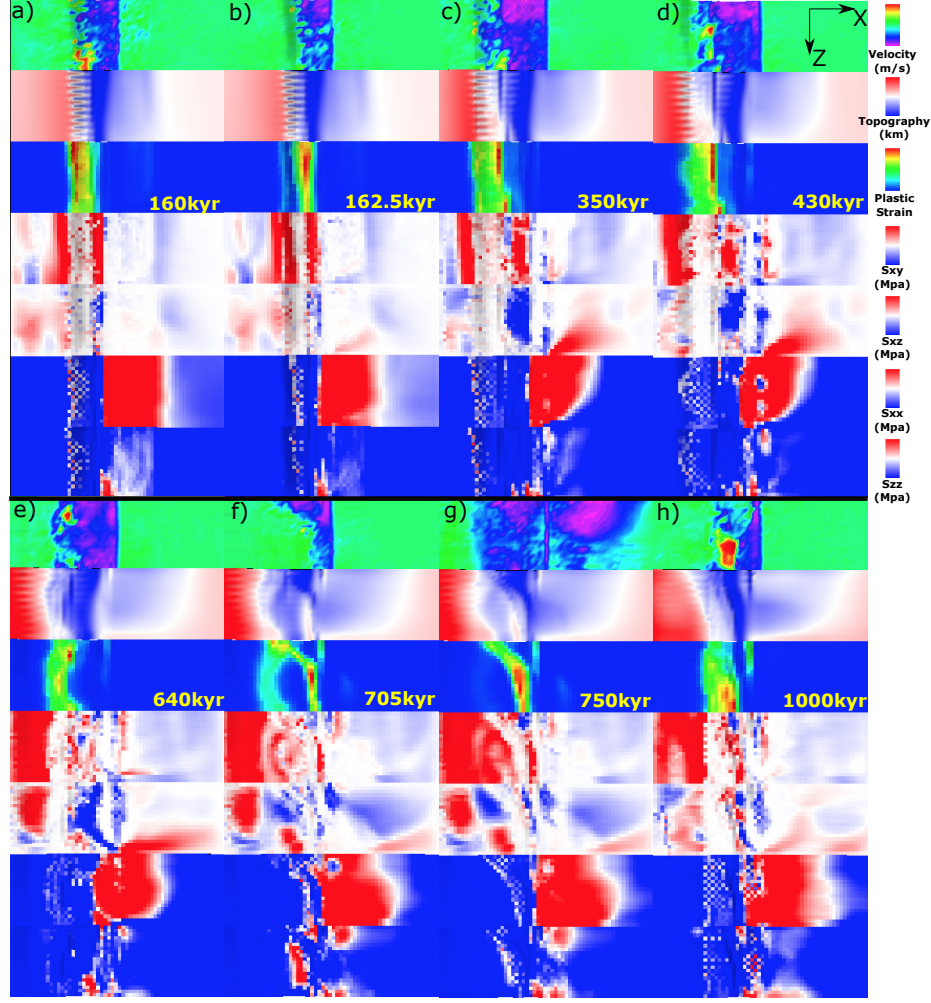


Figure 37: M57LinT1 (Table 2) faulting and stress evolution with respect to time.

axis original fault at low Z side. The topography at 1000 kyr (Figure 37.h) is a result of the curved and later connected fault. The frontier of the plastic strain at high Z side soon catch up with that at the low Z side due to the presence of a tensile failure zone at the low Z side that has taken up part of the extension.

3.5.4 M28SqrtT1 versus M58SqrtT1

For description of M28SqrtT1 evolution with respect to time, please refer to Paragraph 2 and Figure 20.

For description of M58SqrtT1 evolution with respect to time, please refer to Paragraph 3.4.2 and Figure 34.

3.5.5 M57SqrtT2 versus M58SqrtT2

For description of M58SqrtT2 evolution with respect to time, please refer to Paragraph 3.4.2 and Figure 35.

The major difference between M57SqrtT2 and M58SqrtT2 is that M57SqrtT2 keeps faulting at the same side of the ridge axis while M58SqrtT2 alternates.

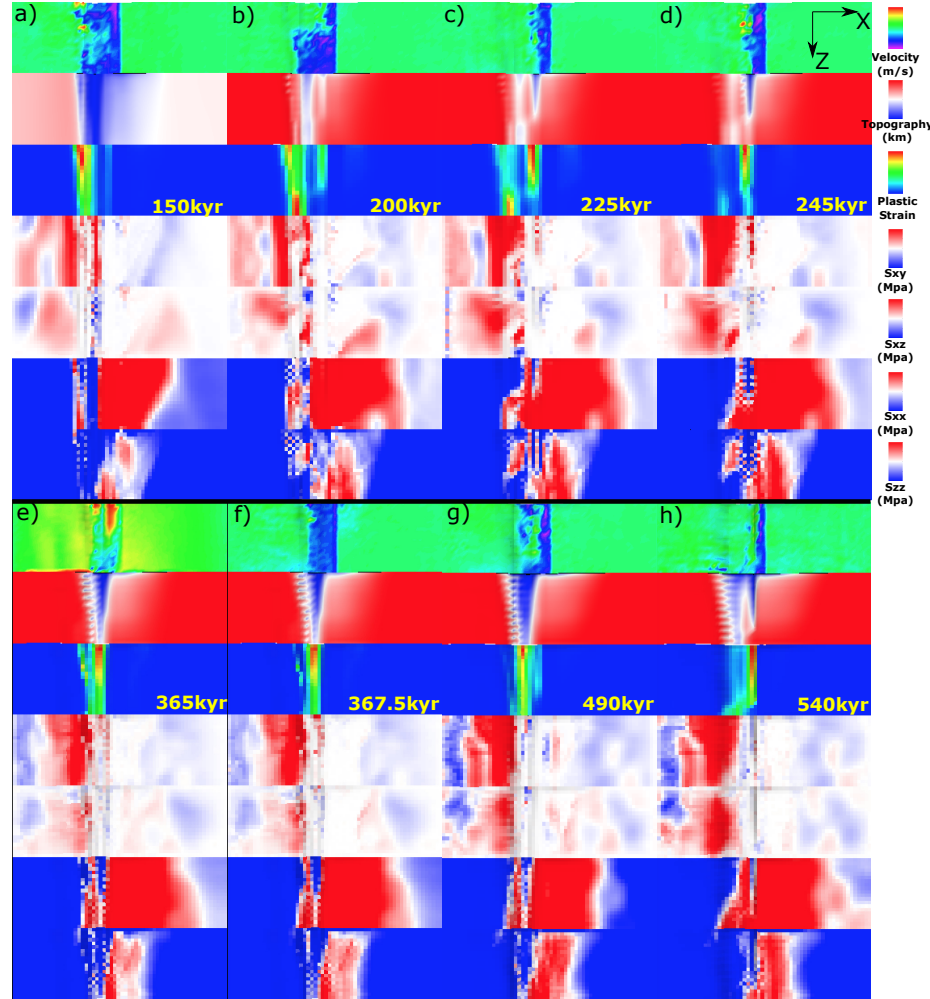


Figure 38: M57SqrtT2 (Table 2) faulting and stress evolution with respect to time.

M57SqrtT2 For M57SqrtT2, there are totally six small scale cut back happen at 282.5 kyr, 290 kyr, 365 kyr, 452.5 kyr, 482.5 kyr and 540 kyr respectively (the model stops at 540 kyr). As shown in Figure 38, the fault keeps on the left hand side of the ridge axis. At 200 kyr (Figure 38.b), a new near ridge axis high angle normal fault begin to evolve

and take the place of the initial one. As the fault evolve, a transient stage of discontinuous abyssal hill is produced at the low Z side as seen at 225 kyr (Figure 38.c). The fault propagate toward high Z side and cut through the plate at \sim 245 kyr (Figure 38.d) when sawtooth shape topography at the low Z side (2nd row) is created by sawtooth shape σ_{xx} (6th row) and σ_{zz} (7th row). Between 365 kyr (Figure 38.e) and 367.5 kyr (Figure 38.f), there is a cut back. At 490 kyr (Figure 38.g), there is new near ridge axis antithetic fault on the hanging wall which terminates the old fault and develops into a vertical near ridge axis tensile failure as seen at 540 kyr (Figure 38.h).

3.6 Summary of Results

There are several behaviors that are controlled by the model parameters. Generally, only M58 models with type 2 weakening produce alternating faults on both side of the ridge axis. All the models show corrugations. As for faulting patterns in terms of evolution frequency, usually Square root is more dynamic than Sinusoidal than Linear, M58 is more dynamic than M57 than M28.

Following tables are a summery of the model behaviors with respect to different setup parameters.

Table 3: Model behaviors in short.

A	Alternating Fault	C	Corrugation	SL	Shear Topography Low
NA	Not Alternating	SF	Secondary Fault on one side	CB	Cut Back
DD	Double Dome	AM	Atlantis Massif Shape		

Based on the 11 models with M variation, we observed eight first-order behaviors as shown in Table 3.

Table 4: Linear functional form.

M range Type \	M28	M57	M58
Type one	NA; C; SL; SF _{1500 kyr} ; DD	NA; C; SF _{1380 kyr} ; CB _{330 kyr} ; AM(opposite z)	
Type two			

Table 5: Sinusoidal functional form.

M range Type \	M28	M57	M58
Type one	NA; C; SL; SF _{995 kyr}	NA; C; SL; SF _{760 kyr; 1320 kyr} ; CB _{520 kyr} ; AM	NA; C; SL; CB _{510 kyr} ; SF _{760 kyr; 1140 kyr; 1990 kyr}
Type two		NA; C; SL; SF _{680 kyr} ; CB _{905 kyr}	A _{450 kyr; 600 kyr} ; C(only at low M); CB _{990 kyr}

Table 6: Square root functional form.

M range Type \	M28	M57	M58
Type one	NA; C; SL; CB _{205 kyr; 330 kyr; 1025 kyr}		NA; C _{1770 kyr} (due to shear with dif wave length); SF _{860 kyr} (high M); SF _{1190 kyr} (low M)(Dog Bone); SF _{1690 kyr}
Type two		NA; C; SF _{435 kyr; 1060 kyr} ; CB _{585 kyr} ; CB _{735 kyr} ; CB _{910 kyr} ; CB _{970 kyr}	A _{550 kyr; 920 kyr} ; C; CB _{400 kyr}

4 Discussion

Generally, all models forms a median valley that deepens and widens toward the lower M side (Figure 8) except the reference model with constant $M = 0.8$ (Figure 13). The topography observed in our models, to the first order, is controlled by the spatial and temporal distributions of faulting and to the second order, results from elastically deformation (e.g. The gradual deepening and widening of the median valley; The bending of the crust at the footwall side of the detachment fault results in a domal shape of the fault interface as a mechanism for producing the dome shape of OCCs).

The pattern of the deformation (faulting and elastic deformation) is controlled by the evolving stress in the crust in terms of its distribution and magnitude. The stress evolution is a result of the interaction processes between tectonics and magmatism. Due to constant seafloor spreading, tensional stress orthogonal to the ridge-axis in the crust keeps accumulating. At the same time, along ridge-axis varying diking partially accommodates the stress from far field extension and perturbs the homogeneity state of stress distribution along the ridge-axis. Accumulated stress will be largely released when the tensile or shear failures establish.

Since the model behavior is very complicated. We will focus on the effects being brought by the along ridge-axis variation in diking. Thus, it is worth considering a thought experiment with two end members: One, the along ridge-axis coupling is rigid, so that even along ridge axis variation in M exist, once a fault determined to develop, it will cut through the whole model domain along the ridge-axis(Z-axis) simultaneously. The other end member is that there is totally no coupling along the ridge-axis. So that each slice of crossection profile across the ridge behave separately without being influenced by its neighbour to a extreme that the model behavior is just a combination of 20 pseudo-2D models piled up along ridge-axis with their own M . (IMPORTANT: this suggests the importance and urgency for making clear conclusion and results description for previous pseudo-2D models results. However, one difficulty here is that the characteristic fault off-

set ΔX_c is different between 2D and 3D models.)

4.1 Discussion on Reference models

4.2 Fault Alteration

4.2.1 Trade-off between bending and weakening

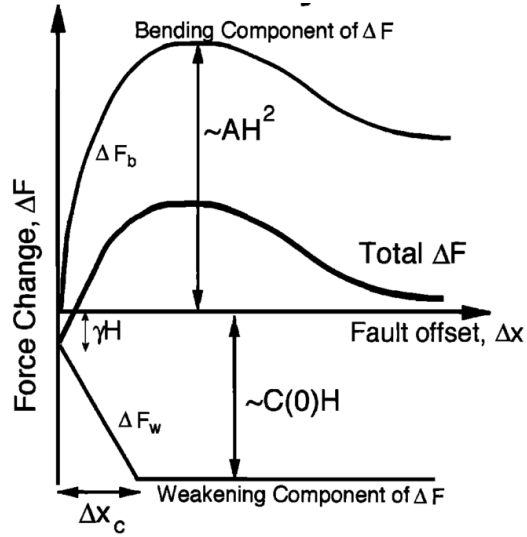


Figure 39: Trade-off between change in bending force ΔF_b and weakening in the fault interface ΔF_w . H is the thickness of the brittle crust and γ is the size of initial weak perturbation and A defines the maximum bending force change. (For more details, please refer to [Lavier et al., 2000])

Before we move on to each of the pairs, the framework studied by [Lavier et al., 2000] needs to be mentioned here for better understanding the model behaviors observed in our model results. There is a trade-off between change in bending force ΔF_b as a function of fault offset ΔX and force change ΔF_w as a function of ΔX due to strain weakening. As described in [Lavier et al., 2000], higher characteristic fault offset (ΔX_c) or slower strain weakening results in multiple faults rather than only one fault lasting. Whether conjugate fault and even multiple faults can be produced depends on the local stress condition. The strength weakening of the existed fault combines with how much bending force resists the fault to keep offsetting play a major role in determining the stress state at the other ar-

eas. As the sea-floor keeps spreading and ΔX increasing, the change in bending force ΔF_b increases and the strength at the fault interface decreases due to weakening ΔF_w (Figure 39). If the net force change $\Delta F = \Delta F_b + \Delta F_w$ is positive, it means that it is getting harder and harder to maintain the existing fault and stress will begin to accumulate at the other areas which eventually break another fault. ΔF_b initially increases fast with respect to ΔX and then when the breakaway bends over, it reaches its peak value and begins to decrease a little and maintains at a constant value. If the strain weakening is fast enough that the net effect force ΔF is always negative, then most of the stress will be released by the existing fault and thus no conjugate or multiple faults will be created.

Our model results verify this analysis that only Type two weakening (slower weakening with higher ΔX_c) can produce an alternating normal fault on the conjugate plate.

Based on the previous experience in pseudo-2D models and [Lavier et al., 2000], when $M > 0.5$, the frequency of normal faulting alternation is higher for higher characteristic fault offset (ΔX_c) of Type two weakening compared to Type one weakening. However, for the reference model two, M88ConT2 (Table 2), interesting enough, when comparing pseudo-2D and 3D models with Type two weakening under case of $M = 0.8$, even though the 3D Model has a larger ΔX_c of 1km than that of pseudo-2D model of 0.5km, the 3D model M88ConT2 has a lower frequency of faulting alternation. Since M is constant 0.8 along the ridge-axis, the effect of along ridge coupling that resists alternation need not be considered. One possibility is that the resisting bending force increase in a higher rate than linear with respect to increasing the length of the ridge segment (Z_{max} km).

4.2.2 Alternating on conjugate plate

The fault alternation behavior observed in pseudo-2D models in cases $M > 0.5$ is much more complicated in 3D models. The results show that only Type two weakening with M58 will result in an alternating faulting pattern. *^{XT}:integrate the area of $M > 0.5$ with*

respect to Z to see if there is any quantatative analysis available.

4.2.3 Secondary near-axis normal fault

The secondary near axis high angle normal fault is another common observation of the models. As shown in Figure 8, at the ridge axis with $M > 0.5$ (i.e. $Z > 10$), the existing normal fault will be pushed away from the ridge-axis due to excessive diking, as its mechanism has been mentioned in the introduction chapter, another new near axis normal fault is created at around 650kyr. As it evolves, the initial detachment fault becomes inactive (the transparent view of plastic strain shown in the right corner inset of time 880kyr). This secondary fault creates another dome and its composition is more likely to be volcanic rather than ultramafic, however, as it evolves, if it can last long, lower crust and upper mantle material can be exhumed to the surface. The composition of the domes observed at Kane magamullions is similar to this mechanism that ultramafic Babel dome is on the West and crustal inside-corner high on the East.

4.2.4 Effect of along ridge-axis coupling

The along ridge-axis coupling allowed the normal fault at the high M side ($M > 0.5$) to last for a long time and become a detachment that can produce an OCC. This behavior is different from previous 2D studies that only $M=0.3 \sim 0.5$ can make OCCs and it also provides an alternative explanation for reconciling the gap between 2D model and observation described in [Olive et al., 2010]. Instead of magma injecting below brittle ductile transition, even injecting in the crust, due to along ridge coupling, model can still create OCC for high magma supply. Find the observation evidence for high M OCC from refs of Olive2010. As mentioned in the abstract of Olive2010, ref4-11 show a spectrum of magma supply.

4.3 Corrugations

There are two contributing factors, for one, trans-extenstional stresses are created due to offset of the breakaway as well as the variation in fault displacements along the ridge axis; for the other, the variation of the positions of the terminations of the detachment faults along the ridge-axis creates anastomosing faults that is mentioned in [Smith et al., 2014]. This anastomosing faulting behavior is largely responsible for corrugations in our models.

The stress at the tips of the breakaways is generally tensional in both parallel and orthogonal directions to the ridge-axis. (Figure 27.f,g)

4.3.1 Wavelength of corrugations

4.4 Influence of healing

4.5 Comparing model results with nature observation

4.5.1 Cut back at 13°N Mid-Atlantic Ridge (M28SqrtT1)

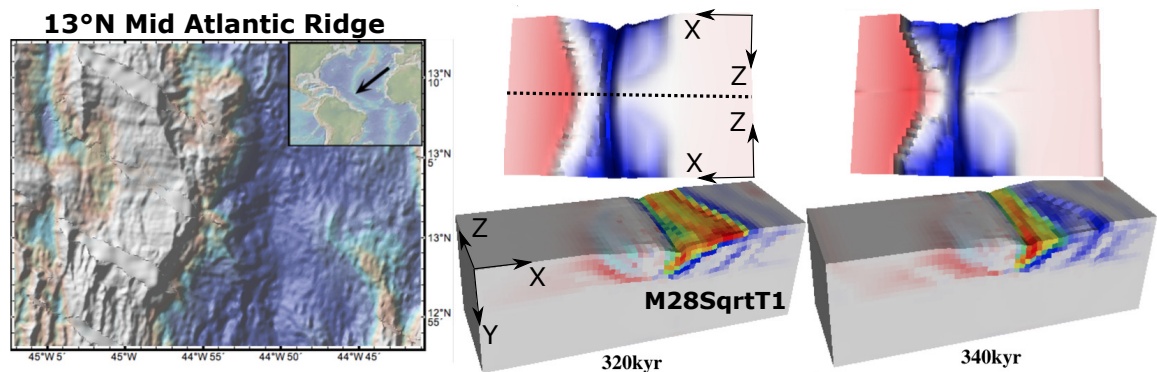


Figure 40: Comparing nature observation at 13°N Mid-Atlantic Ridge to the Cut back behavior of model M28SqrtT1. The model topography is a mirror symetric flip according to the dash line, it reveals the case of M varies in a square root functional form from 0.2 to 0.8 to 0.2. For discussion on cut back formation mechanism, please refer to Section ???. The bathymetry is from GeoMapApp [Ryan et al., 2009].

The cut back behavior in M28SqrtT1 model creates a fault scarp of $\sim 1\text{km}$ in relief,

40km in length along the Z axis. Note that the fault scarp corresponds to initial formed breakaway. The topography at 13°N Mid-Atlantic Ridge also has a fault scarp with very similar geometry with ~1km in relief. Due to the variation in diking along the ridge-axis, a sandglass shape of median valley is also produced in the model where the narrowest center corresponds to the region with high magma supply ($M=0.8$). This sandglass shape is also frequently observed in the nature along the Mid-Atlantic Ridges.

4.5.2 Double dome at 23°N Mid-Atlantic Ridge (Kane Megamullions) (Several models)

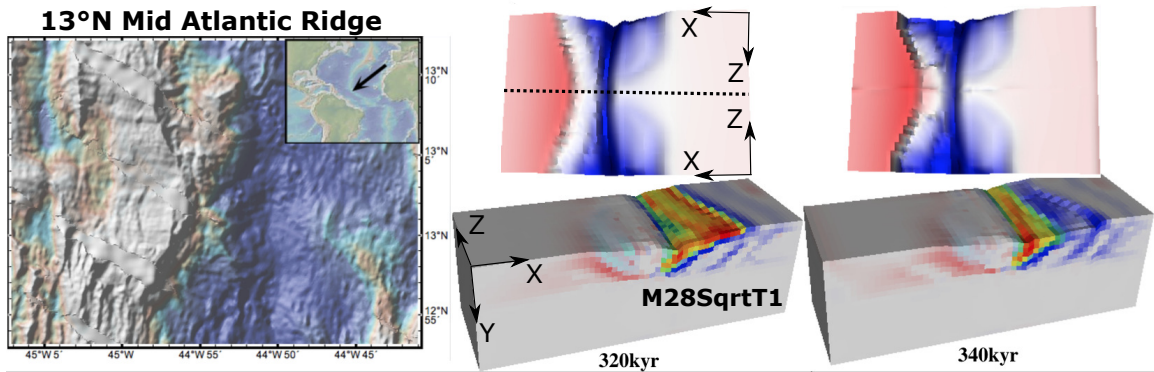


Figure 41: Comparing nature observation at 13°N Mid-Atlantic Ridge to the Cut back behavior of model M28SqrtT1. The model topography is a mirror symmetric flip according to the dash line, it reveals the case of M varies in a square root functional form from 0.2 to 0.8 to 0.2. For discussion on cut back formation mechanism, please refer to Section ??.

4.5.3 Atlantis Massif Shape at 30°N Mid-Atlantic Ridge ()

4.5.4 Shear low

4.5.5 Corrugations

4.6 Model Limitation

4.6.1 Fixed thermal structure effects and justification

Thermal conduction rate for $\kappa = 6\text{mm}^2/\text{s}$ material is $1.8\text{e}5 \text{ km/Myr}$, four magnitude faster compared to spreading rate of 2.5km/Myr .

4.7 Recommendation for Future Research

5 Conclusions

Bibliography

- G. Baines, M. J. Cheadle, B. E. John, and J. J. Schwartz. The rate of oceanic detachment faulting at atlantis bank, sw indian ridge. *Earth and Planetary Science Letters*, 273(1-2):105–114, Aug. 2008. ISSN 0012821X. doi: 10.1016/j.epsl.2008.06.013.
- R. Buck, L. Lavier, and A. Poliakov. Modes of faulting at mid-ocean ridges. *Nature*, 434(7034):719–23, 2005. ISSN 1476-4687. doi: 10.1038/nature03358.
- S. M. Carbotte, D. K. Smith, M. Cannat, and E. M. Klein. Tectonic and magmatic segmentation of the global ocean ridge system : a synthesis of observations. *Geological Society of London*, 2015.
- Y. J. Chen and J. Lin. Mechanisms for the formation of ridge-axis topography at slow-spreading ridges: A lithospheric-plate flexural model. *Geophysical Journal International*, 136:8–18, 1999. ISSN 0956540X. doi: 10.1046/j.1365-246X.1999.00716.x.
- E. Choi, L. Lavier, and M. Gurnis. Thermomechanics of mid-ocean ridge segmentation. *Physics of the Earth and Planetary Interiors*, 171(1-4):374–386, Dec. 2008. ISSN 00319201. doi: 10.1016/j.pepi.2008.08.010.
- C. M. R. Fowler. *The solid earth: an introduction to global geophysics*. Cambridge University Press, 2004.
- S. Kirby and A. K. Kronenberg. Rheology of the lithosphere: Selected topics. *Reviews of Geophysics*, 25(6):1219–1244, 1987.
- L. L. Lavier, W. R. Buck, and A. N. B. Poliakov. Factors controlling normal fault offset in an ideal brittle layer. *Journal of Geophysical Research*, 105(B10):23431, 2000. doi: 10.1029/2000JB900108.
- J. Lin, G. M. Purdy, H. Schouten, J.-C. Sempere, and C. Zervas. Evidence from gravity

data for focused magmatic accretion along the Mid-Atlantic Ridge. *Nature*, 344:627–632, 1990. ISSN 0028-0836. doi: 10.1038/344627a0.

J.-A. Olive, M. D. Behn, and B. E. Tucholke. The structure of oceanic core complexes controlled by the depth distribution of magma emplacement. *Nature Geoscience*, 3(7):491–495, June 2010. ISSN 1752-0894. doi: 10.1038/ngeo888.

J.-a. Olive, M. D. Behn, and L. C. Malatesta. Modes of extensional faulting controlled by surface processes. *Geochemistry Geophysics Geosystems*, pages 1–9, 2014. doi: 10.1002/2014GL061507.

W. B. F. Ryan, S. M. Carbotte, J. O. Coplan, S. O’Hara, A. Melkonian, R. Arko, R. A. Weissel, V. Ferrini, A. Goodwillie, F. Nitsche, J. Bonczkowski, and R. Zemsky. Global multi-resolution topography synthesis. *Geochemistry, Geophysics, Geosystems*, 10, 2009. ISSN 15252027. doi: 10.1029/2008GC002332.

D. K. Smith, H. Schouten, H. J. B. Dick, J. R. Cann, V. Salters, H. R. Marschall, F. Ji, D. Yoerger, A. Sanfilippo, R. Parnell-turner, C. Palmiotto, A. Zhelezov, H. Bai, W. Junkin, B. Urann, S. Dick, M. Sulanowska, P. Lemmond, and S. Curry. Development and evolution of detachment faulting along 50 km of the mid-atlantic ridge near 16.5°n. *Geochemistry Geophysics Geosystems*, pages 4692–4711, 2014. doi: 10.1002/2014GC005563. Received.

M. Tolstoy, A. J. Harding, and J. A. Orcutt. Crustal Thickness on the Mid-Atlantic Ridge: Bull’s-Eye Gravity Anomalies and Focused Accretion. *Science*, 262(October):726–729, 1993. ISSN 0036-8075. doi: 10.1126/science.262.5134.726.

B. E. Tucholke, M. D. Behn, W. R. Buck, and J. Lin. Role of melt supply in oceanic detachment faulting and formation of megamullions. *Geology*, 36(6):455, 2008. ISSN 0091-7613. doi: 10.1130/G24639A.1.

D. L. Turcotte and G. Schubert. *Geodynamics*. Cambridge, 2002.